Effective radiative forcing in the aerosol–climate model CAM5.3-MARC-ARG

Benjamin S. Grandey[1], Daniel Rothenberg[2], Alexander Avramov[2,3], Qinjian Jin[2], Hsiang-He Lee[1], Xiaohong Liu[4], Zheng Lu[4], Samuel Albani[5,6], and Chien Wang[2,1]

5   [1]Center for Environmental Sensing and Modeling, Singapore-MIT Alliance for Research and Technology, Singapore
[2]Center for Global Change Science, Massachusetts Institute of Technology, Cambridge, Massachusetts, USA
[3]Department of Environmental Sciences, Emory University, Atlanta, Georgia, USA
[4]Department of Atmospheric Science, University of Wyoming, Laramie, Wyoming, USA
[5]Department of Earth and Atmospheric Sciences, Cornell University, Ithaca, New York, USA
10 [6]Laboratoire des Sciences du Climat et de l'Environnement, LSCE/IPSL, CEA-CNRS-UVSQ, Gif-sur-Yvette, France

Correspondence to: Benjamin S. Grandey (benjamin@smart.mit.edu)

Abstract. We quantify the effective radiative forcing (ERF) of anthropogenic aerosols modelled by the aerosol–climate model CAM5.3-MARC-ARG. CAM5.3-MARC-ARG is a new configuration of the Community Atmosphere Model version 5.3 (CAM5.3) in which the default aerosol module has been replaced by the two-Moment, Multi-Modal, Mixing-state-
15 resolving Aerosol model for Research of Climate (MARC). CAM5.3-MARC-ARG uses the default ARG aerosol activation scheme, consistent with the default configuration of CAM5.3. We compute differences between simulations using year-1850 aerosol emissions and simulations using year-2000 aerosol emissions in order to assess the radiative effects of anthropogenic aerosols. We compare the aerosol column burdens, cloud properties, and radiative effects produced by CAM5.3-MARC-ARG with those produced by the default configuration of CAM5.3, which uses the modal aerosol module
20 with three log-normal modes (MAM3). Compared with MAM3, we find that MARC produces stronger cooling via the direct radiative effect, stronger cooling via the surface albedo radiative effect, and stronger warming via the cloud longwave radiative effect. The global mean cloud shortwave radiative effect is similar between MARC and MAM3, although the regional distributions differ. Overall, MARC produces a global mean net ERF of -1.75 ± 0.04 W m^{-2}, which is stronger than the global mean net ERF of -1.57 ± 0.04 W m^{-2} produced by MAM3. The regional distribution of ERF also differs
25 between MARC and MAM3, largely due to differences in the regional distribution of the cloud shortwave radiative effect. We conclude that the specific representation of aerosols in global climate models, including aerosol mixing state, has important implications for climate modelling.

1 Introduction

Aerosol particles influence the earth's climate system by perturbing its radiation budget. There are three primary
30 mechanisms by which aerosols interact with radiation. First, aerosols interact directly with radiation by scattering and absorbing solar and thermal infrared radiation (Haywood and Boucher, 2000). Second, aerosols interact indirectly with

radiation by perturbing clouds, by acting as the cloud condensation nuclei on which cloud droplets form and the ice nuclei that facilitate freezing of cloud droplets (Fan et al., 2016; Rosenfeld et al., 2014): for example, an aerosol-induced increase in cloud cover would lead to increased scattering of "shortwave" solar radiation and increased absorption of "longwave" thermal infrared radiation. Third, aerosols can influence the albedo of the earth's surface (Ghan, 2013): for example,

5   deposition of absorbing aerosol on snow reduces the albedo of the snow, causing more solar radiation to be absorbed at the earth's surface.

The "effective radiative forcing" (ERF) of anthropogenic aerosols, defined as the top-of-atmosphere radiative effect caused by anthropogenic emissions of aerosols and aerosol precursors, is often used to quantify the radiative effects of aerosols (Boucher et al., 2013). The anthropogenic aerosol ERF is approximately equivalent to "the radiative flux

10   perturbation associated with a change from preindustrial to present-day [aerosol emissions], calculated in a global climate model using fixed sea surface temperature" (Haywood and Boucher, 2000). This approach "allows clouds to respond to the aerosol while [sea] surface temperature is prescribed" (Ghan, 2013).

The primary tools available for investigating the anthropogenic aerosol ERF are state-of-the-art global climate models. However, there is widespread disagreement among these models, especially regarding the magnitude of

15   anthropogenic aerosol ERF (Quaas et al., 2009; Shindell et al., 2013). Of particular importance are model parameterizations related to aerosol–cloud interactions, such as the aerosol activation scheme (Rothenberg et al., 2017), the choice of autoconversion threshold radius (Golaz et al., 2011), and constraints on the minimum cloud droplet number concentration (Hoose et al., 2009). The detailed representation of aerosols also likely plays an important role, because the aerosol particle size and chemical composition determine hygroscopicity and hence influence aerosol activation (Petters and Kreidenweis,

20   2007).

The magnitude of the ERF of anthropogenic aerosols is highly uncertain: estimates of the global mean anthropogenic aerosol ERF range from -1.9 to -0.1 W m^{-2} (Boucher et al., 2013). Since the present-day anthropogenic aerosol ERF partially masks the warming effects of anthropogenic greenhouse gases, the large uncertainty in the anthropogenic aerosol ERF is a major source of uncertainty in estimates of equilibrium climate sensitivity and projections of

25   future climate (Andreae et al., 2005). Furthermore, the anthropogenic aerosol ERF is regionally inhomogeneous, adding another source of uncertainty in climate projections (Shindell, 2014). The regional inhomogeneity of the anthropogenic aerosol ERF has likely also influenced rainfall patterns during the 20th century (Wang, 2015). In order to improve understanding of current and future climate, including rainfall patterns, it is necessary to improve understanding of the magnitude and regional distribution of the anthropogenic aerosol ERF.

30   In this manuscript, we investigate the uncertainty in anthropogenic aerosol ERF associated with the representation of aerosols in global climate models. In particular, we assess the aerosol radiative effects produced by a new configuration of the Community Atmosphere Model version 5.3 (CAM5.3). In this new configuration – CAM5.3-MARC-ARG – the default modal aerosol module has been replaced with the two-Moment, Multi-Modal, Mixing-state-resolving Aerosol model

for Research of Climate (MARC). We compare the aerosol radiative effects produced by CAM5.3-MARC-ARG with those produced by the default modal aerosol module in CAM5.3.

2 Methodology

2.1 Modal aerosol modules (MAM3 and MAM7)

5　The Community Earth System Model version 1.2.2 (CESM 1.2.2) contains the Community Atmosphere Model version 5.3 (CAM5.3). Within CAM5.3, the default aerosol module is a modal aerosol module which parameterizes the aerosol size distribution with three log-normal modes (MAM3), each assuming a total internal mixture of a set of fixed chemical species (Liu et al., 2012). Optionally, a more detailed modal aerosol module with seven log-normal modes (MAM7) (Liu et al., 2012) can be used instead of MAM3. More recently, a version containing four modes (MAM4) (Liu et al., 2016) has also

10　been coupled to CAM5.3, but we do not consider MAM4 in this study.

　　　The seven modes included in MAM7 are Aitken, accumulation, primary carbon, fine soil dust, fine sea salt, coarse soil dust, and coarse sea salt. Within each of these modes, MAM7 simulates the mass mixing ratios of internally-mixed sulfate, ammonium, primary organic carbon, secondary organic carbon, black carbon, soil dust, and sea salt (Liu et al., 2012).

15　　　In MAM3, four simplifications are made: first, the primary carbon mode is merged into the accumulation mode; second, the fine soil dust and fine sea salt modes are also merged into the accumulation mode; third, the coarse soil dust and coarse sea salt modes are merged to form a single coarse mode; and fourth, ammonium is implicitly included via sulfate and is no longer explicitly simulated. As a result, MAM3 simulates just three modes: Aitken, accumulation, and coarse. This reduces the computational expense of the model.

20　　　In this manuscript, we often refer to MAM3 and MAM7 collectively as "MAM". The MAM-simulated aerosols interact with radiation, allowing aerosol direct and semi-direct effects to be represented. The aerosols can act as cloud condensation nuclei via the ARG aerosol activation scheme (Abdul-Razzak and Ghan, 2000); sulfate and dust also act as ice nuclei. Via such activation, the aerosols are coupled to the stratiform cloud microphysics (Gettelman et al., 2010; Morrison and Gettelman, 2008), allowing aerosol indirect effects on stratiform clouds to be represented. These indirect effects

25　dominate the anthropogenic aerosol ERF in CAM version 5.1 (CAM5.1) (Ghan et al., 2012). In comparison with many other global climate models, the anthropogenic aerosol ERF in CAM5.1 is relatively strong (Shindell et al., 2013).

2.2 The two-Moment, Multi-Modal, Mixing-state-resolving Aerosol model for Research of Climate (MARC)

The two-Moment, Multi-Modal, Mixing-state-resolving Aerosol model for Research of Climate (MARC), which is based on the aerosol microphysical scheme developed by Ekman et al. (2004, 2006) and Kim et al. (2008), simulates the evolution of

30　mixtures of aerosol species. Previous versions of MARC have been used both in cloud-resolving model simulations (Ekman et al., 2004, 2006, 2007; Engström et al., 2008; Wang, 2005a, 2005b) and in global climate model simulations (Ekman et al.,

2012; Kim et al., 2008, 2014). Recently, an updated version of MARC has been coupled to CAM5.3 within CESM1.2.2 (Rothenberg et al., 2017).

In contrast to MAM, MARC tracks the number concentrations and mass concentrations of both externally-mixed and internally-mixed aerosol modes with assumed lognormal size distributions. The externally-mixed modes include three pure sulfate modes (nucleation, Aitken, and accumulation), pure organic carbon, and pure black carbon. The internally-mixed modes include mixed organic carbon plus sulfate and mixed black carbon plus sulfate. In the mixed organic carbon plus sulfate mode, it is assumed that the organic carbon and sulfate are mixed homogeneously within each particle; in the mixed black carbon plus sulfate mode, it is assumed that each particle contains a black carbon core surrounded by a sulfate shell. Sea salt and mineral dust are represented using sectional single-moment schemes, each with four size bins (Albani et al., 2014; Mahowald et al., 2006; Scanza et al., 2015).

Sea salt emissions follow the default scheme used by MAM (Liu et al., 2012), based on simulated wind speed and sea surface temperature. Dust emissions follow the tuning of Albani et al. (Albani et al., 2014), based on simulated wind speed and soil properties, including soil moisture and vegetation cover. Emissions of sulfur dioxide, dimethyl sulfide, primary sulfate aerosol, organic carbon aerosol, black carbon aerosol, and volatile organic compounds (such as isoprene and monoterpene) are prescribed.

The aerosol removal processes represented by MARC – including nucleation scavenging by both stratiform and convective clouds, impaction scavenging by precipitation, and dry deposition – are based on aerosol size and mixing state. Resuspension of aerosols from evaporation of cloud and rain drops is also included. Further details about the formulation of MARC, as well as validation of its simulated aerosol fields compared with observations, can be found in the body and Supplement of Rothenberg et al. (2017).

Whereas previous versions of MARC represented only direct interactions between aerosols and radiation (Kim et al., 2008), an important feature of the new version of MARC is that the aerosols also interact indirectly with radiation via clouds. The MARC-simulated aerosols interact with stratiform cloud microphysics via the default stratiform cloud microphysics scheme (Gettelman et al., 2010; Morrison and Gettelman, 2008), as would be the case for the default MAM3 configuration of CAM5.3. Various aerosol activation schemes can be used with MARC (Rothenberg et al., 2017), including versions of a recently-developed scheme based on polynomial chaos expansion (Rothenberg and Wang, 2016, 2017). The choice of activation scheme can substantially influence the ERF (Rothenberg et al., 2017). In order to facilitate comparison between the MAM and MARC aerosol modules, we have chosen to keep the activation scheme constant in this study: as is the case for the MAM simulations, the ARG activation scheme (Abdul-Razzak and Ghan, 2000) is also used for the MARC simulations. We refer to this configuration as "CAM5.3-MARC-ARG".

2.3 Simulations

In order to compare results from MAM3, MAM7, and MARC, five CAM5.3 simulations are performed:

1. "MAM3_2000", which uses MAM3 with year-2000 aerosol (including aerosol precursor) emissions;

Atmospheric
Chemistry
and Physics
Discussions

2. "MAM7_2000", which uses MAM7 with year-2000 aerosol emissions;

3. "MARC_2000", which uses MARC with year-2000 aerosol emissions;

4. "MAM3_1850", which uses MAM3 with year-1850 aerosol emissions; and

5. "MARC_1850", which uses MARC with year-1850 aerosol emissions.

5   The three simulations using year-2000 emissions, referred to as the "year-2000 simulations", facilitate comparison of aerosol fields and cloud fields; the two simulations using year-1850 emissions, referred to as the "year-1850 simulations", further facilitate analysis of the aerosol radiative effects produced by MAM3 and MARC. There is no MAM7 simulation using year-1850 aerosol emissions, due to a lack of year-1850 emissions files for MAM7. The only difference between the year-2000 simulations and the year-1850 simulations is the aerosol (including aerosol precursor) emissions. In the figures and
10   discussion of results, "2000-1850" and "Δ" both refer to differences between the year-2000 simulation and the year-1850 simulation for a given aerosol module (e.g. MARC_2000-MARC_1850).

The prescribed emissions for both MAM and MARC follow the default MAM emissions files, described in the Supplement of Liu et al. (2012), based on Lamarque et al. (2010). This differs from Rothenberg et al. (2017), who used different emissions of organic carbon aerosol, black carbon aerosol, and volatile organic compounds. In this study, we
15   deliberately use identical emissions for MAM and MARC so that the influence of emissions inventories can be minimised when the results are compared.

For the MAM simulations, the aerosol emissions from some sources follow a vertical profile (Liu et al., 2012). For the MARC simulations, sulfur emissions follow the same vertical profile as for MAM; but all organic carbon, black carbon, and volatile organic compounds are emitted at the surface. 2.5% of the sulfur dioxide is emitted as primary sulfate. Mineral
20   dust and sea salt emissions are not prescribed, being calculated "online".

CESM 1.2.2, with CAM5.3, is used for all simulations. Greenhouse gas concentrations and sea surface temperatures (SSTs) are prescribed using year-2000 climatological values, based on the "F_2000_CAM5" component set. CAM5.3 is run at a horizontal resolution of 1.9°×2.5° with 30 levels in the vertical direction. Clean-sky radiation diagnostics are included, facilitating diagnosis of the direct radiative effect. The Cloud Feedback Model Intercomparison
25   Project (CFMIP) Observational Simulator Package (COSP) (Bodas-Salcedo et al., 2011) is switched on, although the COSP diagnostics are not analysed in this manuscript.

Each simulation is run for 32 years, and the first two years are excluded as spin-up. Hence, a period of 30 years is analysed.

2.4 Diagnosis of radiative effects

30   Pairs of prescribed-SST simulations, with differing aerosol emissions, facilitate diagnosis of anthropogenic aerosol ERF via the "radiative flux perturbation" approach (Haywood et al., 2009). When "clean-sky" radiation diagnostics are available, the ERF can be decomposed into contributions from different radiative effects (Ghan, 2013). (We use the term "radiative

Atmospheric
Chemistry
and Physics
Discussions

forcing" only when referring to ERF, defined as the radiative flux perturbation between a simulation using year-1850 emissions and a simulation using year-2000 emissions; we use the term "radiative effect" more generally.)

The shortwave effective radiative forcing (ERF_{SW}) can be decomposed as follows:

$$ERF_{SW} = \Delta DRE_{SW} + \Delta CRE_{SW} + \Delta SRE_{SW} \qquad (1)$$

5 where Δ refers to the 2000-1850 difference, DRE_{SW} is the direct radiative effect, CRE_{SW} is the clean-sky shortwave cloud radiative effect, and ΔSRE_{SW} is the 2000-1850 surface albedo radiative effect. These components are defined as follows:

$$ERF_{SW} = \Delta F \qquad (2)$$

$$DRE_{SW} = (F - F_{clean}) \qquad (3)$$

$$CRE_{SW} = (F_{clean} - F_{clean,clear}) \qquad (4)$$

10 $$\Delta SRE_{SW} = \Delta F_{clean,clear} \qquad (5)$$

where F is the net shortwave flux at top-of-atmosphere (TOA), F_{clean} is the clean-sky net shortwave flux at TOA, and $F_{clean,clear}$ is the clean-sky clear-sky net shortwave flux at TOA. ("Clear-sky" refers to a hypothetical situation where clouds do not interact with radiation; "clean-sky" refers to a hypothetical situation where aerosols do not directly interact with radiation.)

15 The longwave effective radiative forcing (ERF_{LW}) is calculated as follows:

$$ERF_{LW} = \Delta L \approx \Delta(L - L_{clear}) = \Delta CRE_{LW} \qquad (6)$$

where L is the net longwave flux at TOA, L_{clear} is the clear-sky net longwave flux at TOA, and CRE_{LW} is the longwave cloud radiative effect. Eq. (6) assumes that aerosols and surface albedo changes do not influence the longwave flux at TOA, so that $\Delta L_{clear} \approx 0$.

20 The net effective radiative forcing (ERF_{SW+LW}) is simply the sum of ERF_{SW} and ERF_{LW}:

$$ERF_{SW+LW} = \Delta(F + L) = ERF_{SW} + ERF_{LW} \approx ERF_{SW} + \Delta CRE_{LW}. \qquad (7)$$

All the quantities mentioned in Eqs. (1)–(7) are calculated at TOA.

We also consider absorption by aerosols in the atmosphere (AAA_{SW}), defined as follows:

$$AAA_{SW} = (F - F_{clean}) - (F^{surface} - F_{clean}^{surface}) \qquad (8)$$

25 where $F^{surface}$ is the net shortwave flux at the earth's surface, and $F_{clean}^{surface}$ is the clean-sky net shortwave flux at the earth's surface.

3 Results

We focus on model output fields relating to different components of the ERF, taking each component in turn: the direct radiative effect, the cloud radiative effect, and the surface albedo radiative effect. When discussing each of these 30 components, we also discuss related model field; for example, in the section discussing the direct radiative effect we also

consider other fields related to direct aerosol–radiation interactions. But first, to provide context for the discussion of the radiative effects, we examine the aerosol column burdens.

3.1 Aerosol column burdens

An aerosol column burden, also referred to as a loading, reveals the total mass of a given aerosol species in an atmospheric
5   column. The advantage of column burdens is that they are relatively simple to understand, facilitating comparison between the different aerosol modules. However, when comparing the column burdens, it is important to remember that information about aerosol size distribution and aerosol mixing state is hidden. Information about the vertical distribution is also hidden, because the burdens are integrated throughout the atmospheric column.

3.1.1 Total sulfate aerosol burden

10   Figure 1a–c shows the total sulfate aerosol burden ($Burden_{SO4}$) for the year-2000 simulations. For all three aerosol modules, year-2000 $Burden_{SO4}$ is highest in the Northern Hemisphere subtropics and mid-latitudes, especially near source regions with high anthropogenic emissions of sulfur dioxide. Year-2000 $Burden_{SO4}$ is much lower in the Southern Hemisphere, especially over the remote Southern Ocean and Antarctica. In general, there is close agreement between MAM and MARC over the Northern Hemisphere tropics and the Southern Hemisphere. However, over the Northern Hemisphere
15   subtropics and mid-latitudes, year-2000 $Burden_{SO4}$ is generally lower for MARC compared with MAM3. Interestingly, over the Northern Hemisphere subtropics, the zonal means are very similar between MAM7 and MARC.

       Figure 1d–f shows $\Delta Burden_{SO4}$, the 2000-1850 difference in $Burden_{SO4}$. Both MAM3 and MARC produce widespread positive values of $\Delta Burden_{SO4}$ across the Northern Hemisphere and also across South America, Africa, and Oceania. For both MAM3 and MARC, global mean $\Delta Burden_{SO4}$ accounts for more than half of global mean year-2000
20   $Burden_{SO4}$, indicating that anthropogenic sulfur emissions are responsible for more than half of the global burden of sulfate aerosol.

3.1.2 Total organic carbon aerosol burden

Figure 2a–c shows the total organic carbon aerosol burden ($Burden_{OC}$) for the year-2000 simulations. For both MAM3 and MARC, year-2000 $Burden_{OC}$ peaks in the tropics, especially sub-Saharan Africa and South America, due to emissions from
25   wildfires. The impact of anthropogenic emissions of organic carbon aerosol is evident over South Asia and East Asia. Biogenic emissions of isoprene and monoterpene also contribute to $Burden_{OC}$. In general, year-2000 $Burden_{OC}$ is higher for MARC than it is for MAM. This suggests that the organic carbon aerosol lifetime is longer for MARC compared with MAM, consistent with the differing representations of mixing state influencing wet removal efficiency: MAM3 assumes that all organic carbon aerosol is internally-mixed with other species, whereas MARC also includes a pure organic carbon aerosol
30   mode with very low hygroscopicity.

Over the major emissions regions of organic carbon aerosol, MAM3 and MARC both produce positive values of $\Delta Burden_{OC}$, the 2000-1850 difference in $Burden_{OC}$ (Fig. 2d–f). However, negative values of $\Delta Burden_{OC}$ are found over North America, especially for MAM3. These 2000-1850 differences arise due to changes in both wildfire emissions and anthropogenic emissions of organic carbon aerosol between year-1850 and year-2000. Although emissions of some volatile

5   organic compounds do change between year-1850 and year-2000, emissions of isoprene and monoterpene remain unchanged so these species are unlikely to contribute to $\Delta Burden_{OC}$.

3.1.3 Total black carbon aerosol burden

Figure 3a–c shows the total black carbon aerosol burden ($Burden_{BC}$) for the year-2000 simulations. For both MAM3 and MARC, year-2000 $Burden_{BC}$ is high over sub-Saharan Africa and South America, as was the case for $Burden_{OC}$, due to

10 large emissions of black carbon aerosol from wildfires. However, in contrast to $Burden_{OC}$, the peak in zonal mean year-2000 $Burden_{BC}$ occurs in the Northern Hemisphere subtropics and mid-latitudes, due to anthropogenic emissions of black carbon aerosol over East Asia, South Asia, Europe, and North America. In the tropics, year-2000 $Burden_{BC}$ is generally similar between MAM and MARC. Outside of the tropics, year-2000 $Burden_{BC}$ for MARC is generally higher than that for MAM, especially over remote regions far away from sources. This suggests that the black carbon aerosol lifetime is longer

15 for MARC than it is for MAM, likely due to the low hygroscopicity of the pure black carbon aerosol mode in MARC.

MAM3 and MARC produce similar increases in $Burden_{BC}$ between year-1850 and year-2000, as indicated by positive values of $\Delta Burden_{BC}$ (Fig. 3d–f). For MARC, positive values of $\Delta Burden_{BC}$ are found over even remote ocean regions, consistent with a longer black carbon lifetime for MARC compared with MAM3.

3.1.4 Total sea salt aerosol burden

20 Figure 4a–c shows the total sea salt aerosol burden ($Burden_{salt}$) for the year-2000 simulations. For both MAM3 and MARC, year-2000 $Burden_{salt}$ is highest over ocean areas with strong surface wind speeds (Fig. S9b, c). Over land, year-2000 $Burden_{salt}$ is very low, suggesting that the sea salt aerosol generally has a relatively short lifetime, as expected due to the large particle size and high hygroscopicity. Year-2000 $Burden_{salt}$ is very similar between MAM3 and MARC. This is not surprising, because MARC uses the same sea salt emissions parameterization as MAM3 does.

25 For both MAM3 and MARC, $\Delta Burden_{salt}$, the 2000-1850 difference in $Burden_{salt}$ (Fig. 4e, f), appears to be positively correlated with the 2000-1850 difference in surface wind speeds (Fig. S9e, f). Changes in precipitation rate (Fig. S8e, f) likely also influence $Burden_{salt}$, because precipitation efficiently removes sea salt aerosol from the atmosphere. However, it should be noted that the 2000-1850 differences in $Burden_{salt}$, surface wind speed, and precipitation rate are both relatively small and often statistically insignificant across most of the world. If an interactive dynamical ocean were to

30 be used, allowing SSTs to respond to the anthropogenic aerosol ERF, it is likely that we would find much larger 2000-1850 differences in surface wind speed, precipitation rate, and $Burden_{salt}$.

Atmospheric
Chemistry
and Physics
Discussions
Open Access
EGU

3.1.5 Total dust aerosol burden

Figure 5a–c shows the total dust aerosol burden ($Burden_{dust}$) for the year-2000 simulations. Dust emission primarily occurs over desert areas, especially the Sahara Desert, so year-2000 $Burden_{dust}$ is highest directly over and downwind of these desert source regions. Year-2000 $Burden_{dust}$ is much larger for MARC, which follows Albani et al., (2014), compared with

5   MAM. The largest differences between MAM3 and MARC appear to occur directly over the desert source regions, suggesting that differences in dust emission drive the differences in year-2000 $Burden_{dust}$ – if this is the case, dust emission is far higher for MARC compared with MAM over the Sahara, Middle East, and East Asian deserts, while the opposite may be true over southern Africa and Australia. However, differences in the lifetime of dust aerosol may also contribute to the differences in year-2000 $Burden_{dust}$ between MAM and MARC. We expect the dust aerosol lifetime to be longer for

10 MARC compared with MAM3, because MAM3 assumes internal mixing of dust with sulfate and sea salt within the coarse mode, thereby increasing the wet removal rate (Liu et al., 2012), while MARC assumes that dust aerosol remains pure (with no internal mixing).

     $\Delta Burden_{dust}$, the 2000-1850 difference in $Burden_{dust}$ (Fig. 5d–f), reveals that $Burden_{dust}$ decreases between year-1850 and year-2000, especially over the Sahara Desert. Both MAM3 and MARC produce a similar zonal mean decrease in

15 $Burden_{dust}$. The reasons for the 2000-1850 changes in $Burden_{dust}$ are unclear, although changes in surface wind speed (Fig. S9d–f), influencing emission, and changes in precipitation rate (Fig. S8d–f), influencing lifetime, likely play a role. As we noted above when discussing the sea salt burden, if an interactive dynamical ocean were to be used, it is likely that we would find much larger 2000-1850 differences in surface wind speed, precipitation rate, and $Burden_{dust}$.

3.2 Aerosol–radiation interactions and the direct radiative effect

20 ### 3.2.1 Aerosol optical depth

Aerosols scatter and absorb shortwave radiation, leading to extinction of incoming solar radiation. Before considering the direct radiative effect, we first look at aerosol optical depth (AOD), a measure of the total extinction due to aerosols in an atmospheric column.

     Figure 6a–c shows AOD for the year-2000 simulations. For both MAM and MARC, zonal mean year-2000 AOD

25 peaks in the Northern Hemisphere subtropics, driven by emission of dust from deserts, especially the Sahara Desert. Over other regions, both anthropogenic aerosol emissions and natural aerosol emissions, including emissions of sea salt, contribute to year-2000 AOD. The year-2000 AOD values for MARC are often much lower than those for MAM3, especially over subtropical ocean regions. Rothenberg et al. (2017) have also previously noted that the AOD for MARC is generally lower than that retrieved from the MODerate Resolution Imaging Spectroradiometer (MODIS; Collection 5.1); but it should be

30 noted that differences in spatial-temporal sampling (Schutgens et al., 2017, 2016) have not been accounted for. The differences between the aerosol burdens for MAM3 and MARC, discussed above, are insufficient to explain the differences

in year-2000 AOD. Hence it is likely that differences in the optical properties of the MARC aerosols and the MAM3 aerosols are responsible for the fact that MARC generally produces lower values of AOD.

Positive 2000-1850 differences in $Burden_{SO4}$, $Burden_{OC}$, and $Burden_{BC}$, discussed above, drive positive values of ΔAOD, the 2000-1850 difference in AOD (Fig. 6d–f). As was the case for year-2000 AOD, ΔAOD produced by MARC is
5   generally much lower than ΔAOD produced by MAM3.

3.2.2 Direct radiative effect

Figure 7a–c shows the direct radiative effect (DRE_{SW}) for the year-2000 simulations. DRE_{SW} reveals the influence of direct interactions between radiation and aerosols on the net shortwave flux at TOA (Eq. (3)). Aerosols that scatter shortwave radiation efficiently, such as sulfate, generally contribute to negative values of DRE_{SW}, indicating a cooling effect on the
10   climate system; aerosols that absorb shortwave radiation, such as black carbon, generally contribute to positive values of DRE_{SW}, indicating a warming effect on the climate system. Other factors, such as the presence of clouds, the vertical distribution of aerosols relative to clouds, and the albedo of the earth's surface, also play a role in determining DRE_{SW} (Stier et al., 2007). Due to these factors – especially the differing impact of scattering and absorbing aerosols and variations in the albedo of the earth's surface – large values of AOD may not necessarily correspond to large values of DRE_{SW}. Having said
15   that, for both MAM3 and MARC, the regional distribution of year-2000 DRE_{SW} shares some similarities with that of year-2000 AOD. Over dark ocean surfaces in the subtropics, scattering by aerosols drives negative values of year-2000 DRE_{SW}. The impact of dust on year-2000 DRE_{SW} differs between MAM3 and MARC, likely due to differing optical properties: for MAM3, absorption by dust drives positive values over the bright surface of the Sahara Desert, while little radiative impact is evident downwind over the dark surface of the tropical Atlantic Ocean; for MARC, scattering by dust drives negative values
20   over the tropical Atlantic Ocean, while little radiative impact is evident over the Sahara Desert.

For MAM3, ΔDRE_{SW}, the 2000-1850 difference in DRE_{SW}, is relatively weak at all latitudes (Fig. 7d, e), with a global mean of only -0.02 ± 0.01 W m^{-2}, due to the cooling effect of anthropogenic sulfur emissions being offset by the warming effect of increased black carbon aerosol emissions (Ghan et al., 2012). In contrast, for MARC, ΔDRE_{SW} reveals a relatively strong cooling effect across much of the Northern Hemisphere (Fig. 7d, f), especially near anthropogenic sources
25   of sulfur emissions, leading to a global mean ΔDRE_{SW} of -0.18 ± 0.01 W m^{-2}.

3.2.3 Absorption by aerosols in the atmosphere

Figure 8a–c shows the absorption of shortwave radiation by aerosols in the atmosphere (AAA_{SW}; Eq. (8)) for the year-2000 simulations. Consideration of AAA_{SW}, which reveals heating of the atmosphere by aerosols, complements consideration of DRE_{SW}. For example, over the Sahara Desert, we noted above that the dust aerosol in MARC exerts only a weak direct
30   radiative effect at TOA (Fig. 7c); however, Fig. 8c reveals that the dust aerosol in MARC leads to strong heating of the atmosphere. For both MAM and MARC, year-2000 AAA_{SW} is largest near emission sources of dust, especially over the

Sahara Desert where year-2000 $Burden_{dust}$ is particularly high, showing that dust is the primary driver of year-2000 AAA_{SW}. Further away from the dust emission source regions, year-2000 AAA_{SW} is spatially correlated with year-2000 $Burden_{BC}$, showing that black carbon aerosol also contributes to year-2000 AAA_{SW}. Despite the fact that year-2000 $Burden_{dust}$ and $Burden_{BC}$ are larger for MARC compared with MAM, year-2000 AAA_{SW} is generally weaker for MARC compared with
5 MAM3: this difference in year-2000 AAA_{SW} is likely due to differences in the aerosol optical properties, associated with different handling of dust and black carbon aerosol mixing state between MAM3 and MARC.

ΔAAA_{SW}, the 2000-1850 difference in AAA_{SW} (Fig. 8d–f), generally follows the same regional distribution as $\Delta Burden_{BC}$, showing that changes in emissions of black carbon aerosol dominate ΔAAA_{SW}. Although dust dominates year-2000 AAA_{SW}, changes in dust emission exert only a relatively small influence on ΔAAA_{SW}. As with year-2000 AAA_{SW},
10 ΔAAA_{SW} is generally weaker for MARC compared with MAM3.

3.3 Aerosol–cloud interactions and the cloud radiative effects

3.3.1 Cloud condensation nuclei concentration

Many aerosol particles have the potential to become the cloud condensation nuclei (CCN) on which water vapour condenses to form cloud droplets. Figure 9a–c shows the CCN concentration at a fixed supersaturation of 0.1% (CCN_{conc}) in the lower
15 troposphere for the year-2000 simulations. Corresponding results showing year-2000 CCN_{conc} near the surface and in the mid-troposphere are shown in Figs. S1a–c and S2a–c of the Supplement. Looking at year-2000 CCN_{conc} across these different vertical levels, we make two initial observations: first, for both MAM and MARC, year-2000 CCN_{conc} is generally higher in the Northern Hemisphere; second, year-2000 CCN_{conc} is generally much lower for MARC compared with MAM.

When we look in more detail at the regional distribution of year-2000 CCN_{conc} for MAM3, and compare this to the
20 column burden results, we notice that locations with high CCN_{conc} have either high $Burden_{SO4}$ or high $Burden_{OC}$. This suggests that, for MAM3, the organic carbon aerosol – internally-mixed with other species with high hygroscopicity – contributes to efficient CCN, consistent with two previous MAM3-based studies that found that organic carbon emissions from wildfires can exert a strong influence on clouds (Grandey et al., 2016a; Jiang et al., 2016).

In contrast, for MARC, the regional distribution of year-2000 CCN_{conc} closely resembles that of $Burden_{SO4}$ but
25 does not resemble that of $Burden_{OC}$. This suggests that, for MARC, the organic carbon aerosol – much of which remains in a pure organic carbon aerosol mode with very low hygroscopicity – is not an efficient source of CCN.

If we look at the results for ΔCCN_{conc}, the 2000-1850 difference in CCN_{conc} (Figs. 9d–f, S1d–f, and S2d–f), similar deductions about sulfate aerosol and organic carbon aerosol can be made as were made above. For MAM3, the regional distribution of ΔCCN_{conc} reveals that changes in the availability of CCN are associated with both $\Delta Burden_{SO4}$ and
30 $\Delta Burden_{OC}$. For MARC, the regional distribution of ΔCCN_{conc} is associated with $\Delta Burden_{SO4}$, but is not closely associated with $\Delta Burden_{OC}$. For both MAM and MARC, ΔCCN_{conc} is generally positive, revealing increasing availability of CCN between year-1850 and year-2000. The absolute increase is smaller for MARC than for MAM.

Atmospheric
Chemistry
and Physics
Discussions

Open Access

EGU

It is important to note that these CCN_{conc} results are for a fixed supersaturation of 0.1%; but as pointed out by Rothenberg et al. "*all* aerosol [particles] are potentially CCN, given an updraft sufficient enough in strength to drive a high-enough supersaturation such that they grow large enough to activate" (Rothenberg et al., 2017). Furthermore, the number of CCN that are actually activated is influenced by competition for water vapour among various types of aerosol particles,

5   which depends on the details of the aerosol population including size distribution and mixing state. When aerosol particles with a lower hygroscopicity rise alongside aerosol particles with a higher hygroscopicity in a rising air parcel, the latter would normally be activated first at a supersaturation that is much lower than the one required for the former to become activated; the consequent condensation of water vapour to support the diffusive growth of the newly formed cloud particles would effectively lower the saturation level of the air parcel and further reduce the chance for the lower hygroscopicity

10   aerosol particles to be activated (Rothenberg and Wang, 2016, 2017). In other words, CCN_{conc} at a fixed supersaturation is not necessarily a good indicator of the number of CCN that are actually activated, because activation depends on specific environmental conditions and the details of the aerosol population present. In an aerosol model such as MAM3 that includes only internally-mixed modes, the hygroscopicity of a given mode is derived by volume weighting through all the included aerosol species and is therefore not very sensitive to changes in the chemical composition of the mode. In contrast, MARC

15   explicitly handles mixing state and thus hygroscopicity of each individual type of aerosol.

3.3.2 Column-integrated cloud droplet number concentration

The availability of CCN influences cloud microphysics via the formation of cloud droplets. Figure 10a–c shows column-integrated cloud droplet number concentration ($CDNC_{column}$) for the year-2000 simulations. For MAM, year-2000 $CDNC_{column}$ is generally higher in the Northern Hemisphere, with very high values occurring over regions with abundant

20   sulfate aerosol or organic carbon aerosol providing abundant CCN. In contrast, for MARC there is no strong inter-hemispheric asymmetry in year-2000 $CDNC_{column}$: there appears to be no influence from organic carbon aerosol, consistent with the CCN_{conc} results discussed above; and the influence of sulfate aerosol appears weaker than for MAM. Interestingly, there is good agreement between MAM and MARC over the Southern Ocean: for both MAM and MARC, sea salt appears to have a substantial influence on year-2000 $CDNC_{column}$.

25   When we look at $\Delta CDNC_{column}$, the 2000-1850 difference in $CDNC_{column}$ (Fig. 10d–f), we see that anthropogenic emissions generally drive increases in $CDNC_{column}$, as expected. The absolute increase is smaller for MARC than for MAM.

3.3.3 Grid-box cloud liquid and cloud ice water paths

In addition to influencing cloud microphysical properties (such as cloud droplet number concentration), the availability of CCN and ice nuclei influence cloud macrophysical properties (such as cloud water path). Figure 11a–c shows grid-box

30   cloud liquid water path (WP_{liquid}) for the year-2000 simulations. Year-2000 WP_{liquid} is highest in the tropics and mid-latitudes. The regional distribution of year-2000 WP_{liquid} is similar to that of total cloud fractional coverage (Fig. S4a–c).

Atmospheric
Chemistry
and Physics
Discussions

The regional distribution of year-2000 WP_{liquid} for MARC is very similar to that for MAM. However, compared with MAM, MARC produces slightly higher year-2000 WP_{liquid} in the Southern Hemisphere mid-latitudes, the Southern Hemisphere subtropics, and the Arctic.

Figure 12a–c shows grid-box cloud ice water path (WP_{ice}) for the year-2000 simulations. As with WP_{liquid}, year-2000 WP_{ice} is highest in the tropics and mid-latitudes. The regional distribution of year-2000 WP_{ice} is similar to that of high-level cloud fractional coverage (Fig. S7a–c), and is similar between MAM and MARC. However, year-2000 WP_{ice} is consistently lower for MARC than for MAM. Although MARC and MAM3 are coupled to the same ice and mixed-phase cloud microphysics scheme (Gettelman et al., 2010; Liu et al., 2007), differences in the availability of ice nuclei can arise due to differences in dust and sulfate number concentrations and size distributions. Differences in tuneable parameters, for which observational constraints do not exist, may also play a role: the uncertainties associated with ice nucleation are very large (Garimella et al., 2017).

The 2000-1850 differences in WP_{liquid} and WP_{ice} are shown in Figs. 11d–f and 12d–f. MAM3 produces large increases in WP_{liquid} over Europe, East Asia, Southeast Asia, South Asia, parts of Africa, and northern South America – the regional distribution of ΔWP_{liquid} is similar to the regional distributions of ΔCCN_{conc} and $\Delta CDNC_{column}$. MARC produces large increase in WP_{liquid} over the same regions, and additionally over Australia and North America. Overall, ΔWP_{liquid} is larger for MARC than for MAM3, especially over the Northern Hemisphere mid-latitudes. For MARC, in comparison with MAM3, the relatively strong ΔWP_{liquid} response contrasts with the relatively weak ΔCCN_{conc} response and $\Delta CDNC_{column}$ response.

Globally, for both MAM3 and MARC, the ΔWP_{ice} response is relatively weak (Fig. 12d–f). However, relatively large values of ΔWP_{ice}, both positive and negative, are found regionally. This regional response differs between MAM3 and MARC. For both MAM3 and MARC, it appears that decreases in WP_{ice} correspond to increases in $Burden_{OC}$ (Fig. 2e, f); but this relationship is likely spurious, because organic carbon aerosol does not directly influence ice processes in either aerosol module.

3.3.4 Shortwave cloud radiative effect

Figure 13a–c shows the clean-sky shortwave cloud radiative effect (CRE_{SW}; Eq. (4)) for the year-2000 simulations. Clouds scatter much of the incoming solar radiation, exerting a strong cooling effect on the climate system. This cooling effect is strongest in the tropics and mid-latitudes. The regional distribution of year-2000 CRE_{SW} is strongly negatively correlated with WP_{liquid} and WP_{total} (the total cloud water path; Fig. S3): large values of WP_{liquid} and WP_{total} correspond to a strong cooling effect.

The same applies to ΔCRE_{SW}, the 2000-1850 difference in CRE_{SW} (Fig. 13d–f), which is strongly negatively correlated with ΔWP_{liquid} and ΔWP_{total}: increases in WP_{liquid} and WP_{total} drive a stronger shortwave cloud cooling effect. For both MAM3 and MARC, the cooling effect of ΔCRE_{SW} is strongest in the Northern Hemisphere, particularly regions

with high anthropogenic sulfur emissions, especially East Asia, Southeast Asia, and South Asia. Compared with MAM3, MARC produces a slightly stronger ΔCRE_{SW} response in the mid-latitudes and a slightly weaker ΔCRE_{SW} response in the sub-tropics. Another difference between MAM3 and MARC is the land-ocean contrast: compared with MAM3, MARC often produces a slightly stronger ΔCRE_{SW} response over land but a weaker ΔCRE_{SW} response over ocean.

5   When globally averaged, the global mean ΔCRE_{SW} for MARC (-2.11 ± 0.03 W m^{-2}) is very similar to that for MAM3 (-2.09 ± 0.04 W m^{-2}). Considering the differences between MAM3 and MARC, we find it somewhat surprising that the two aerosol modules produce such a similar global mean ΔCRE_{SW} response, although we have noted differences in the regional distribution.

3.3.5 Longwave cloud radiative effect

10   The cooling effect of CRE_{SW} is partially offset by the warming effect of CRE_{LW} (Eq. (6)), the longwave cloud radiative effect which arises due to absorption of longwave thermal infrared radiation. Figure 14a–c shows CRE_{LW} for the year-2000 simulations. As with the shortwave cooling effect, the longwave warming effect is strongest in the tropics and mid-latitudes, for both MAM and MARC. The regional distribution of year-2000 CRE_{LW} is positively correlated with WP_{ice} (Fig. S12a–c) and high-level cloud fraction (Fig. S7a–c) – high-level ice cloud drives the longwave warming effect.

15   The same is true for ΔCRE_{LW}, the 2000-1850 difference in CRE_{LW} (Fig. 14d–f): changes in high-level ice cloud cover drive changes in the longwave cloud warming effect. For both MAM3 and MARC, ΔCRE_{LW} is positive over much of Southeast Asia, South Asia, the Indian Ocean, the Atlantic Ocean, and Pacific Ocean; ΔCRE_{LW} is negative over much of Africa and parts of South America. When averaged globally, MAM3 produces a global mean ΔCRE_{LW} of $+0.54 \pm 0.02$ W m^{-2}, while MARC produces a stronger global mean of $+0.66 \pm 0.02$ W m^{-2}. Hence ΔCRE_{LW} offsets approximately one

20 quarter to one third of the ΔCRE_{SW} cooling effect.

3.4 The surface albedo radiative effect

In addition to interacting with radiation both directly and indirectly via clouds, aerosols can influence the earth's radiative energy balance via changes to the surface albedo. The surface albedo radiative effect (ΔSRE_{SW}; Eq. (5)), "includes effects of both changes in snow albedo due to deposition of absorbing aerosol, and changes in snow cover induced by deposition and

25 by the other aerosol forcing mechanisms" (Ghan, 2013). For both MAM and MARC, deposition of absorbing aerosol is enabled via the coupling between CAM5 and the land scheme in CESM; and "other aerosol forcing mechanisms" include aerosol-induced changes in precipitation rate. Aerosol-induced changes in column water vapor can also influence the calculation of ΔSRE_{SW}, because $F_{clean,clear}$ is sensitive to near-infrared absorption by water vapour; but the contribution from such changes in column water vapour is small. (ΔSRE_{SW} does not include changes in land use, because the only difference

30 between the year-1850 and year-2000 simulations is the aerosol emissions.)

Figure 15 shows ΔSRE_{SW}, the 2000-1850 surface albedo radiative effect. In the Arctic and high-latitude land regions of the Northern Hemisphere, ΔSRE_{SW} can be relatively large. MAM3 produces a mixture of positive and negative ΔSRE_{SW} values, averaging out to approximately zero globally ($+0.00 \pm 0.02$ W m^{-2}). However, MARC tends to produce mainly negative ΔSRE_{SW} values, averaging out to a global mean of -0.12 ± 0.02 W m^{-2}.

5   The ΔSRE_{SW} response is associated with 2000-1850 changes in snow cover over both land and sea-ice (Fig. S10d–f): increases in snow cover lead to negative ΔSRE_{SW} values, while decreases in snow cover lead to positive ΔSRE_{SW} values. Changes in snow rate (Fig. S11d–f) likely play a major role, explaining much of the snow cover response. Changes in black carbon deposition (Fig. S12d–f), contributing to changes in the mass of black carbon in the top layer of snow (Fig. S13d–f), may also play a role. The mass of black carbon in the top layer of snow is much lower for MARC compared with MAM

10   (Fig. S13a–c); the 2000-1850 difference in the mass of black carbon in the top layer of snow is also much lower for MARC compared with MAM (Fig. S13d–f).

3.5 Net effective radiative forcing

The net effective radiative forcing (ERF_{SW+LW}) – the 2000-1850 difference in the net radiative flux at TOA (Eq. (7)) – is effectively the sum of the radiative effect components we discussed above. Figure 16 shows ERF_{SW+LW}; Table 1

15   summarises the global mean contribution from the different radiative effect components.

In general, the cloud shortwave component, ΔCRE_{SW}, dominates, resulting in negative values of ERF_{SW+LW} across much of the world. In particular, strongly negative values of ERF_{SW+LW}, indicating a large cooling effect, are found near regions with substantial anthropogenic sulfur emissions. The cooling effect is far stronger in the Northern Hemisphere than it is in the Southern Hemisphere. If coupled atmosphere–ocean simulations were to be performed, allowing SSTs to

20   respond, the large inter-hemispheric difference in ERF_{SW+LW} would likely impact inter-hemispheric temperature gradients and hence rainfall patterns (Chiang and Friedman, 2012; Grandey et al., 2016b; Wang, 2015).

Across much of the globe, the net cooling effect of ERF_{SW+LW} produced by MARC is similar to that produced by MAM. However, in the mid-latitudes, MARC produces a stronger net cooling effect, especially over North America, Europe, and northern Asia. Another difference is that MARC appears to exert more widespread cooling over land than

25   MAM does, while the opposite appears to be the case over ocean. These differences in the regional distribution of ERF_{SW+LW} are largely due to differences in the regional distribution of ΔCRE_{SW}. As mentioned in the previous paragraph, rainfall patterns are sensitive to changes in surface temperature gradients. Therefore, if SSTs were allowed to respond to the forcing, the differences in the regional distribution of ERF_{SW+LW} between MARC and MAM may drive differences in rainfall patterns.

30   When averaged globally, MAM3 produces a global mean ERF_{SW+LW} of -1.57 ± 0.04 W m^{-2}; MARC produces a stronger global mean ERF_{SW+LW} of -1.75 ± 0.04 W m^{-2}. The ERF_{SW+LW} produced by CAM5.3-MARC-ARG is particularly strong compared with many other global climate models (Shindell et al., 2013). However, the global mean

ERF_{SW+LW} may become weaker if the inter-annual variability in the wildfire emissions of organic carbon were to be carefully accounted for (Grandey et al., 2016a).

4 Summary and conclusions

The specific representation of aerosols in global climate models, especially the representation of aerosol mixing state, has important implications for aerosol hygroscopicity, aerosol lifetime, aerosol column burdens, aerosol optical properties, and cloud condensation nuclei availability. For example, in addition to internally-mixed modes, MARC also includes a pure organic carbon aerosol mode and a pure black carbon aerosol mode both of which have very low hygroscopicity. The low hygroscopicity of these pure organic carbon and pure black carbon modes likely leads to increased aerosol lifetime compared with the internally-mixed modes. Therefore, far away from emissions sources, the column burdens of organic carbon aerosol and black carbon aerosol are higher for MARC compared with MAM3, which contains only internally-mixed aerosol modes. Furthermore, the representation of aerosol mixing state, and the associated implications for hygroscopicity, strongly influences the ability of the aerosol particles to act as cloud condensation nuclei.

We have demonstrated that changing the aerosol module in CAM5.3 influences both the direct and indirect radiative effects of aerosols. Standard CAM5.3, which uses the MAM3 aerosol module, produces a global mean net ERF of -1.57 ± 0.04 W m^{-2} associated with the 2000-1850 difference in aerosol (including aerosol precursor) emissions; CAM5.3-MARC-ARG, which uses the MARC aerosol module, produces a stronger global mean net ERF of -1.75 ± 0.04 W m^{-2}, a particularly strong cooling effect compared with other climate models (Shindell et al., 2013). As summarised below, the difference in the global mean net ERF is primarily driven by differences in the direct radiative effect and the surface albedo radiative effect; but indirect radiative effects via clouds contribute to differences in the regional distribution of ERF produced by MAM3 and MARC.

By analysing the individual components of the net ERF, we have demonstrated that:

1. The global mean 2000-1850 direct radiative effect produced by MAM3 (-0.02 ± 0.01 W m^{-2}) is close to zero due to the warming effect of black carbon aerosol opposing the cooling effect of sulfate aerosol and organic carbon aerosol. In contrast, the 2000-1850 direct radiative effect produced by MARC is -0.18 ± 0.01 W m^{-2}, with the cooling effect of sulfate aerosol being larger than the warming effect of black carbon aerosol.

2. The global mean 2000-1850 shortwave cloud radiative effect produced by MARC (-2.11 ± 0.03 W m^{-2}) is very similar to that produced by MAM3 (-2.09 ± 0.04 W m^{-2}). However, the regional distribution differs: for MAM3, the cooling peaks in the Northern Hemisphere subtropics; while for MARC, the cooling peaks in the Northern Hemisphere mid-latitudes. The land-ocean contrast also differs: compared with MAM3, MARC often produces stronger cooling over land but weaker cooling over ocean. For both MAM3 and MARC, the 2000-1850 shortwave cloud radiative effect is closely associated with changes in liquid water path.

Atmospheric
Chemistry
and Physics
Discussions
EGU
Open Access

3. The global mean 2000-1850 longwave cloud radiative effect produced by MARC ($+0.66 \pm 0.02$ W m^{-2}) is stronger than that produced by MAM3 ($+0.54 \pm 0.02$ W m^{-2}). For both MAM3 and MARC, the 2000-1850 longwave cloud radiative effect is closely associated with changes in ice water path and high cloud cover.

4. The global mean 2000-1850 surface albedo radiative effect produced by MARC (-0.12 ± 0.02 W m^{-2}) is also stronger than that produced by MAM3 ($+0.00 \pm 0.02$ W m^{-2}). The 2000-1850 surface albedo radiative effect is associated with changes in snow cover.

If climate simulations were to be performed using a coupled atmosphere-ocean configuration of CESM, these differences in the radiative effects produced by MAM3 and MARC would likely lead to differences in the climate response. In particular, the differences in the regional distribution of the radiative effects would likely impact rainfall patterns (Wang, 2015).

In light of these results, we conclude that the specific representation of aerosols in global climate models has important implications for climate modelling. Important interrelated factors include the representation of aerosol mixing state, size distribution, and optical properties.

Appendix A: Computational performance

In order to assess the computational performance of MARC, in comparison with MAM, we have performed six timing simulations. The configuration of these simulations is described in the caption of Table S1.

Before looking at the results, it is worth noting that the default radiation diagnostics differ between MARC and MAM. As highlighted by Ghan (Ghan, 2013), in order to calculate the direct radiative effect of aerosols, a second radiation call is required in order to diagnose "clean-sky" fluxes – in this diagnostic clean-sky radiation call, interactions between aerosols and radiation are switched off. In MARC, these clean-sky fluxes are diagnosed by default. However, in MAM, these clean-sky fluxes are not diagnosed by default, although simulations can be configured to include the necessary diagnostics. The inclusion of the clean-sky diagnostics increases computational expense. Hence, in order to facilitate a fair comparison between MARC and MAM, we have performed two simulations for each aerosol module: one with clean-sky diagnostics switched on, and one with clean-sky diagnostics switched off.

The results from the timing simulations are shown in Table S1. When clean-sky diagnostics are switched off, as would ordinarily be the case for long climate-scale simulations, using MARC increases the computational cost by only 6% compared with a default configuration using MAM3. MAM7 is considerably more expensive. When clean-sky diagnostics are switched on – as is the case for the simulations analysed in this manuscript – the computational cost of MARC is very similar to that of MAM3.

Atmospheric
Chemistry
and Physics
Discussions

Code and data availability

CESM 1.2.2 is available via http://www.cesm.ucar.edu/models/cesm1.2/. The version of MARC used in this study is MARC v1.0.4, archived at https://doi.org/10.5281/zenodo.1117370 (Avramov et al., 2017). Model namelist files, configuration scripts, and analysis code are available via https://github.com/grandey/p17c-marc-comparison/, archived at

5 https://doi.org/10.5281/zenodo.1239247. The MARC input data and the model output data analysed in this paper are archived at https://doi.org/10.6084/m9.figshare.5687812.

Author contributions

AA and DR coupled MARC to CAM5.3 in CESM1.2.2, under the supervision of CW. AA, DR, QJ, and CW contributed to further development of CAM5.3-MARC-ARG, with DR being the primary software maintainer. HHL and BSG contributed

10 to testing of CAM5.3-MARC-ARG. SA contributed dust model code, optical tables, the soil erodibility map, and advice about model configuration. XL led development of MAM3 and MAM7. ZL and XL provided advice about model configuration, especially MAM7. BSG and DR designed the experiment, with contributions from QJ and CW. BSG configured and performed the simulations. BSG, DR, and HHL analysed the results. BSG produced the figures shown in this manuscript. BSG wrote the manuscript, with contributions from all other co-authors. CW provided supervisory

15 guidance throughout the project.

Atmospheric
Chemistry
and Physics
Discussions

Open Access

References

Abdul-Razzak, H. and Ghan, S. J.: A parameterization of aerosol activation: 2. Multiple aerosol types, J. Geophys. Res., 105(D5), 6837–6844, doi:10.1029/1999JD901161, 2000.

Albani, S., Mahowald, N. M., Perry, A. T., Scanza, R. A., Zender, C. S., Heavens, N. G., Maggi, V., Kok, J. F. and Otto-Bliesner, B. L.: Improved dust representation in the Community Atmosphere Model, J. Adv. Model. Earth Syst., 6(3), 541–570, doi:10.1002/2013MS000279, 2014.

Andreae, M. O., Jones, C. D. and Cox, P. M.: Strong present-day aerosol cooling implies a hot future, Nature, 435(7046), 1187–1190, doi:10.1038/nature03671, 2005.

Avramov, A., Rothenberg, D., Jin, Q., Garimella, S., Grandey, B. and Wang, C.: MARC - Model for Research of Aerosols and Climate (version 1.0.4), Zenodo, doi:10.5281/zenodo.1117370, 2017.

Benjamini, Y. and Hochberg, Y.: Controlling the False Discovery Rate: A Practical and Powerful Approach to Multiple Testing, J. R. Stat. Soc. B, 57(1), 289–300, 1995.

Bodas-Salcedo, A., Webb, M. J., Bony, S., Chepfer, H., Dufresne, J.-L., Klein, S. A., Zhang, Y., Marchand, R., Haynes, J. M., Pincus, R. and John, V. O.: COSP: Satellite simulation software for model assessment, Bull. Am. Meteorol. Soc., 92(8), 1023–1043, doi:10.1175/2011BAMS2856.1, 2011.

Boucher, O., Randall, D., Artaxo, P., Bretherton, C., Feingold, G., Forster, P., Kerminen, V.-M., Kondo, Y., Liao, H., Lohmann, U., Rasch, P., Satheesh, S. K., Sherwood, S., Stevens, B. and Zhang, X. Y.: Clouds and Aerosols, in Climate Change 2013: The Physical Science Basis. Contribution of Working Group I to the Fifth Assessment Report of the Intergovernmental Panel on Climate Change, edited by T. F. Stocker, D. Qin, G.-K. Plattner, M. Tignor, S. K. Allen, J. Boschung, A. Nauels, Y. Xia, V. Bex, and P. M. Midgley, Cambridge University Press, Cambridge, United Kingdom and New York, NY, USA., 2013.

Chiang, J. C. H. and Friedman, A. R.: Extratropical Cooling, Interhemispheric Thermal Gradients, and Tropical Climate Change, Annu. Rev. Earth Planet. Sci., 40(1), 383–412, doi:10.1146/annurev-earth-042711-105545, 2012.

Ekman, A. M. L., Wang, C., Wilson, J. and Ström, J.: Explicit simulations of aerosol physics in a cloud-resolving model: a sensitivity study based on an observed convective cloud, Atmos. Chem. Phys., 4(3), 773–791, doi:10.5194/acp-4-773-2004, 2004.

Ekman, A. M. L., Wang, C., Ström, J. and Krejci, R.: Explicit Simulation of Aerosol Physics in a Cloud-Resolving Model: Aerosol Transport and Processing in the Free Troposphere, J. Atmos. Sci., 63(2), 682–696, doi:10.1175/JAS3645.1, 2006.

Ekman, A. M. L., Engström, A. and Wang, C.: The effect of aerosol composition and concentration on the development and anvil properties of a continental deep convective cloud, Q. J. R. Meteorol. Soc., 133(October), 937–948, doi:10.1002/qj.108, 2007.

Ekman, A. M. L., Hermann, M., Groß, P., Heintzenberg, J., Kim, D. and Wang, C.: Sub-micrometer aerosol particles in the upper troposphere/lowermost stratosphere as measured by CARIBIC and modeled using the MIT-CAM3 global climate model, J. Geophys. Res. Atmos., 117(D11), n/a-n/a, doi:10.1029/2011JD016777, 2012.

Engström, A., Ekman, A. M. L., Krejci, R., Ström, J., de Reus, M. and Wang, C.: Observational and modelling evidence of
5   tropical deep convective clouds as a source of mid-tropospheric accumulation mode aerosols, Geophys. Res. Lett., 35(23), L23813, doi:10.1029/2008GL035817, 2008.

Fan, J., Wang, Y., Rosenfeld, D. and Liu, X.: Review of Aerosol–Cloud Interactions: Mechanisms, Significance, and Challenges, J. Atmos. Sci., 73(11), 4221–4252, doi:10.1175/JAS-D-16-0037.1, 2016.

Garimella, S., Rothenberg, D. A., Wolf, M. J., Wang, C. and Cziczo, D. J.: How uncertainty in field measurements of ice
10   nucleating particles influences modeled cloud forcing, J. Atmos. Sci., JAS-D-17-0089.1, doi:10.1175/JAS-D-17-0089.1, 2017.

Gettelman, A., Liu, X., Ghan, S. J., Morrison, H., Park, S., Conley, A. J., Klein, S. A., Boyle, J., Mitchell, D. L. and Li, J.-L. F.: Global simulations of ice nucleation and ice supersaturation with an improved cloud scheme in the Community Atmosphere Model, J. Geophys. Res., 115(D18), D18216, doi:10.1029/2009JD013797, 2010.

15   Ghan, S. J.: Technical Note: Estimating aerosol effects on cloud radiative forcing, Atmos. Chem. Phys., 13(19), 9971–9974, doi:10.5194/acp-13-9971-2013, 2013.

Ghan, S. J., Liu, X., Easter, R. C., Zaveri, R., Rasch, P. J., Yoon, J.-H. and Eaton, B.: Toward a Minimal Representation of Aerosols in Climate Models: Comparative Decomposition of Aerosol Direct, Semidirect, and Indirect Radiative Forcing, J. Clim., 25(19), 6461–6476, doi:10.1175/JCLI-D-11-00650.1, 2012.

20   Golaz, J.-C., Salzmann, M., Donner, L. J., Horowitz, L. W., Ming, Y. and Zhao, M.: Sensitivity of the Aerosol Indirect Effect to Subgrid Variability in the Cloud Parameterization of the GFDL Atmosphere General Circulation Model AM3, J. Clim., 24(13), 3145–3160, doi:10.1175/2010JCLI3945.1, 2011.

Grandey, B. S., Lee, H.-H. and Wang, C.: Radiative effects of interannually varying vs. interannually invariant aerosol emissions from fires, Atmos. Chem. Phys., 16(22), 14495–14513, doi:10.5194/acp-16-14495-2016, 2016a.

25   Grandey, B. S., Cheng, H. and Wang, C.: Transient Climate Impacts for Scenarios of Aerosol Emissions from Asia: A Story of Coal versus Gas, J. Clim., 29(8), 2849–2867, doi:10.1175/JCLI-D-15-0555.1, 2016b.

Haywood, J. and Boucher, O.: Estimates of the direct and indirect radiative forcing due to tropospheric aerosols: A review, Rev. Geophys., 38(4), 513–543, doi:10.1029/1999RG000078, 2000.

Haywood, J., Donner, L., Jones, A. and Golaz, J.-C.: Global Indirect Radiative Forcing Caused by Aerosols: IPCC (2007)
30   and Beyond, in Clouds in the Perturbed Climate System: Their Relationship to Energy Balance, Atmospheric Dynamics, and Precipitation, edited by J. Heintzenberg and R. Charlson, MIT Press., 2009.

Hoose, C., Kristjánsson, J. E., Iversen, T., Kirkevåg, A., Seland and Gettelman, A.: Constraining cloud droplet number concentration in GCMs suppresses the aerosol indirect effect, Geophys. Res. Lett., 36(12), 1–5, doi:10.1029/2009GL038568, 2009.

Jiang, Y., Lu, Z., Liu, X., Qian, Y., Zhang, K., Wang, Y. and Yang, X.-Q.: Impacts of global open-fire aerosols on direct radiative, cloud and surface-albedo effects simulated with CAM5, Atmos. Chem. Phys., 16(23), 14805–14824, doi:10.5194/acp-16-14805-2016, 2016.

Kim, D., Wang, C., Ekman, A. M. L., Barth, M. C. and Rasch, P. J.: Distribution and direct radiative forcing of
5   carbonaceous and sulfate aerosols in an interactive size-resolving aerosol–climate model, J. Geophys. Res., 113(D16), D16309, doi:10.1029/2007JD009756, 2008.

Kim, D., Wang, C., Ekman, A. M. L., Barth, M. C. and Lee, D.-I.: The responses of cloudiness to the direct radiative effect of sulfate and carbonaceous aerosols, J. Geophys. Res. Atmos., 119(3), 1172–1185, doi:10.1002/2013JD020529, 2014.

Lamarque, J.-F., Bond, T. C., Eyring, V., Granier, C., Heil, A., Klimont, Z., Lee, D., Liousse, C., Mieville, A., Owen, B.,
10   Schultz, M. G., Shindell, D., Smith, S. J., Stehfest, E., Van Aardenne, J., Cooper, O. R., Kainuma, M., Mahowald, N., McConnell, J. R., Naik, V., Riahi, K. and van Vuuren, D. P.: Historical (1850–2000) gridded anthropogenic and biomass burning emissions of reactive gases and aerosols: methodology and application, Atmos. Chem. Phys., 10(15), 7017–7039, doi:10.5194/acp-10-7017-2010, 2010.

Liu, X., Penner, J. E., Ghan, S. J. and Wang, M.: Inclusion of Ice Microphysics in the NCAR Community Atmospheric
15   Model Version 3 (CAM3), J. Clim., 20(18), 4526–4547, doi:10.1175/JCLI4264.1, 2007.

Liu, X., Easter, R. C., Ghan, S. J., Zaveri, R., Rasch, P., Shi, X., Lamarque, J.-F., Gettelman, A., Morrison, H., Vitt, F., Conley, A., Park, S., Neale, R., Hannay, C., Ekman, A. M. L., Hess, P., Mahowald, N., Collins, W., Iacono, M. J., Bretherton, C. S., Flanner, M. G. and Mitchell, D.: Toward a minimal representation of aerosols in climate models: description and evaluation in the Community Atmosphere Model CAM5, Geosci. Model Dev., 5(3), 709–739,
20   doi:10.5194/gmd-5-709-2012, 2012.

Liu, X., Ma, P.-L., Wang, H., Tilmes, S., Singh, B., Easter, R. C., Ghan, S. J. and Rasch, P. J.: Description and evaluation of a new four-mode version of the Modal Aerosol Module (MAM4) within version 5.3 of the Community Atmosphere Model, Geosci. Model Dev., 9(2), 505–522, doi:10.5194/gmd-9-505-2016, 2016.

Mahowald, N. M., Lamarque, J.-F., Tie, X. X. and Wolff, E.: Sea-salt aerosol response to climate change: Last Glacial
25   Maximum, preindustrial, and doubled carbon dioxide climates, J. Geophys. Res., 111(D5), D05303, doi:10.1029/2005JD006459, 2006.

Morrison, H. and Gettelman, A.: A New Two-Moment Bulk Stratiform Cloud Microphysics Scheme in the Community Atmosphere Model, Version 3 (CAM3). Part I: Description and Numerical Tests, J. Clim., 21(15), 3642–3659, doi:10.1175/2008JCLI2105.1, 2008.

30 Petters, M. D. and Kreidenweis, S. M.: A single parameter representation of hygroscopic growth and cloud condensation nucleus activity, Atmos. Chem. Phys., 7(8), 1961–1971, doi:10.5194/acp-7-1961-2007, 2007.

Quaas, J., Ming, Y., Menon, S., Takemura, T., Wang, M., Penner, J. E., Gettelman, A., Lohmann, U., Bellouin, N., Boucher, O., Sayer, A. M., Thomas, G. E., McComiskey, A., Feingold, G., Hoose, C., Kristjánsson, J. E., Liu, X., Balkanski, Y., Donner, L. J., Ginoux, P. A., Stier, P., Grandey, B., Feichter, J., Sednev, I., Bauer, S. E., Koch, D., Grainger, R. G.,

Kirkevåg, A., Iversen, T., Seland, Ø., Easter, R., Ghan, S. J., Rasch, P. J., Morrison, H., Lamarque, J.-F., Iacono, M. J., Kinne, S. and Schulz, M.: Aerosol indirect effects – general circulation model intercomparison and evaluation with satellite data, Atmos. Chem. Phys., 9(22), 8697–8717, doi:10.5194/acp-9-8697-2009, 2009.

Rosenfeld, D., Andreae, M. O., Asmi, A., Chin, M., de Leeuw, G., Donovan, D. P., Kahn, R., Kinne, S., Kivekäs, N., Kulmala, M., Lau, W., Schmidt, K. S., Suni, T., Wagner, T., Wild, M. and Quaas, J.: Global observations of aerosol-cloud-precipitation-climate interactions, Rev. Geophys., 52(4), 750–808, doi:10.1002/2013RG000441, 2014.

Rothenberg, D. and Wang, C.: Metamodeling of Droplet Activation for Global Climate Models, J. Atmos. Sci., 73(3), 1255–1272, doi:10.1175/JAS-D-15-0223.1, 2016.

Rothenberg, D. and Wang, C.: An aerosol activation metamodel of v1.2.0 of the pyrcel cloud parcel model: development and offline assessment for use in an aerosol–climate model, Geosci. Model Dev., 10(4), 1817–1833, doi:10.5194/gmd-10-1817-2017, 2017.

Rothenberg, D., Avramov, A. and Wang, C.: On the representation of aerosol activation and its influence on model-derived estimates of the aerosol indirect effect, Atmos. Chem. Phys. Discuss., (August), 1–35, doi:10.5194/acp-2017-680, 2017.

Scanza, R. A., Mahowald, N., Ghan, S., Zender, C. S., Kok, J. F., Liu, X., Zhang, Y. and Albani, S.: Modeling dust as component minerals in the Community Atmosphere Model: development of framework and impact on radiative forcing, Atmos. Chem. Phys., 15(1), 537–561, doi:10.5194/acp-15-537-2015, 2015.

Schutgens, N., Tsyro, S., Gryspeerdt, E., Goto, D., Weigum, N., Schulz, M. and Stier, P.: On the spatio-temporal representativeness of observations, Atmos. Chem. Phys., 17(16), 9761–9780, doi:10.5194/acp-17-9761-2017, 2017.

Schutgens, N. A. J., Partridge, D. G. and Stier, P.: The importance of temporal collocation for the evaluation of aerosol models with observations, Atmos. Chem. Phys., 16(2), 1065–1079, doi:10.5194/acp-16-1065-2016, 2016.

Shindell, D. T.: Inhomogeneous forcing and transient climate sensitivity, Nat. Clim. Chang., 4(4), 274–277, doi:10.1038/nclimate2136, 2014.

Shindell, D. T., Lamarque, J.-F., Schulz, M., Flanner, M., Jiao, C., Chin, M., Young, P. J., Lee, Y. H., Rotstayn, L., Mahowald, N., Milly, G., Faluvegi, G., Balkanski, Y., Collins, W. J., Conley, a. J., Dalsoren, S., Easter, R., Ghan, S., Horowitz, L., Liu, X., Myhre, G., Nagashima, T., Naik, V., Rumbold, S. T., Skeie, R., Sudo, K., Szopa, S., Takemura, T., Voulgarakis, A., Yoon, J.-H. and Lo, F.: Radiative forcing in the ACCMIP historical and future climate simulations, Atmos. Chem. Phys., 13(6), 2939–2974, doi:10.5194/acp-13-2939-2013, 2013.

Stier, P., Seinfeld, J. H., Kinne, S. and Boucher, O.: Aerosol absorption and radiative forcing, Atmos. Chem. Phys., 7(19), 5237–5261, doi:10.5194/acp-7-5237-2007, 2007.

Wang, C.: A modeling study of the response of tropical deep convection to the increase of cloud condensation nuclei concentration: 1. Dynamics and microphysics, J. Geophys. Res., 110(D21), D21211, doi:10.1029/2004JD005720, 2005a.

Wang, C.: A modeling study of the response of tropical deep convection to the increase of cloud condensation nuclei concentration: 2. Radiation and tropospheric chemistry, J. Geophys. Res., 110(D22), D22204,

doi:10.1029/2005JD005829, 2005b.

Wang, C.: Anthropogenic aerosols and the distribution of past large-scale precipitation change, Geophys. Res. Lett., 42(24), 10,876-10,884, doi:10.1002/2015GL066416, 2015.

Wilks, D. S.: "The stippling shows statistically significant gridpoints": How Research Results are Routinely Overstated and

5   Over-interpreted, and What to Do About It, Bull. Am. Meteorol. Soc., doi:10.1175/BAMS-D-15-00267.1, 2016.

Atmospheric
Chemistry
and Physics
Discussions
Open Access

EGU

Tables

Table 1: Area-weighted global mean radiative effects. Combined standard errors are calculated using the annual global mean for each simulation year. The regional distributions of these radiative effects are shown in Figs. 7, 13, 14, 15, and 16. ERF_{SW+LW} is the sum of the other radiative effect components.

5

	2000-1850 radiative effect (W m^{-2})	
	MAM3	MARC
Δ direct radiative effect (ΔDRE_{SW})	- 0.02 ± 0.01	- 0.18 ± 0.01
Δ shortwave cloud radiative effect (ΔCRE_{SW})	- 2.09 ± 0.04	- 2.11 ± 0.03
Δ longwave cloud radiative effect (ΔCRE_{LW})	+ 0.54 ± 0.02	+ 0.66 ± 0.02
Δ surface albedo radiative effect (ΔSRE_{SW})	+ 0.00 ± 0.02	- 0.12 ± 0.02
Net effective radiative forcing (ERF_{SW+LW})	- 1.57 ± 0.04	- 1.75 ± 0.04

Atmospheric
Chemistry
and Physics
Discussions
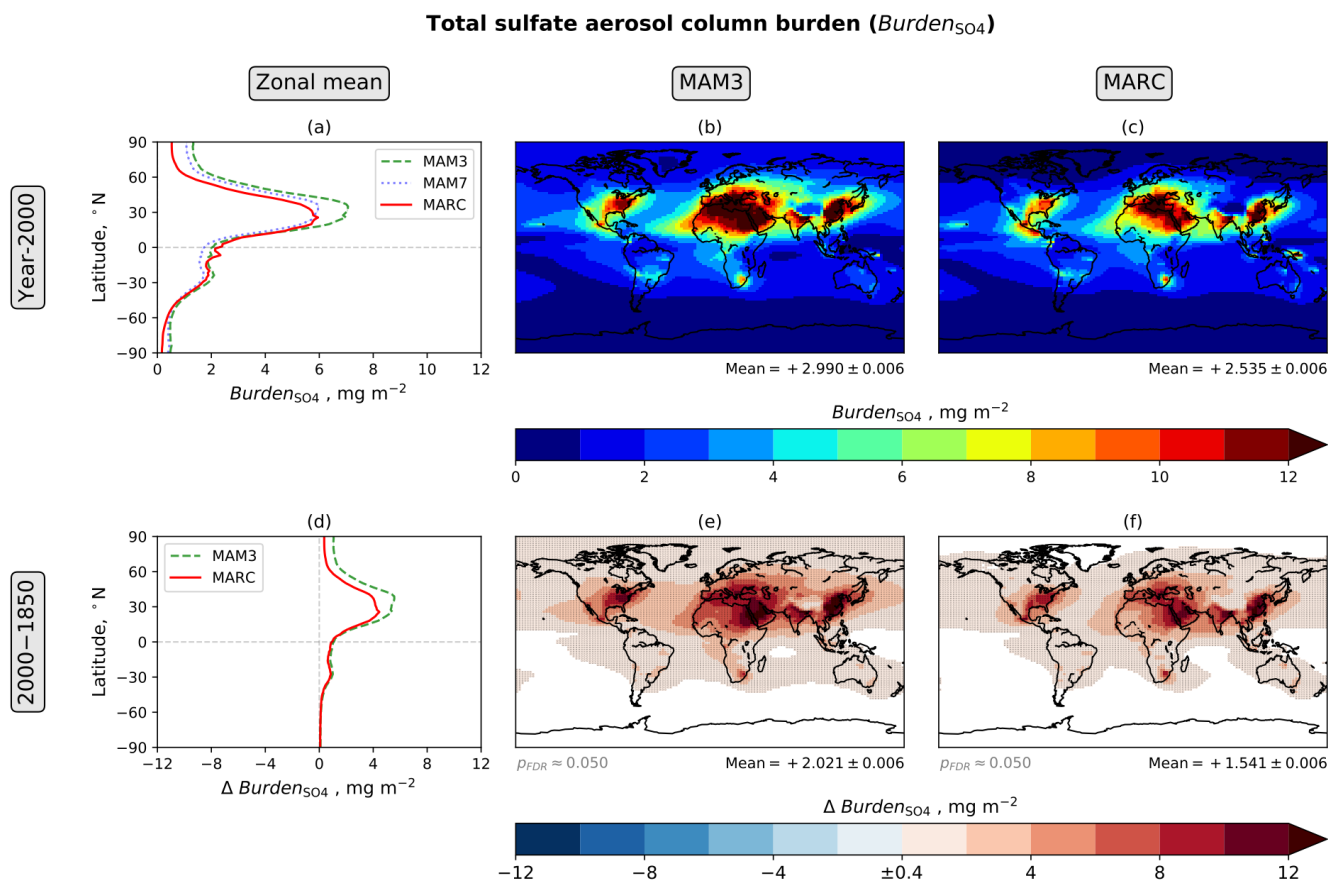
Figures

Figure 1: Annual mean total sulfate aerosol burden ($Burden_{SO4}$). For the zonal means (a, d), the standard errors, calculated using the annual zonal mean for each simulation year, are indicated by shading; but this shading is not visible in Fig. 1, because the standard errors are smaller than the width of the plotted lines. For the maps (b, c, e, f), the area-weighted global mean and associated standard error, calculated using the annual global mean for each simulation year, are shown below each map. For the maps showing 2000-1850 differences (e, f), white indicates differences with a magnitude less than the threshold value in the centre of the colour bar (± 0.4 mg m^{-2}). For locations where the magnitude is greater than this threshold value, stippling indicates differences that are statistically significant at a significance level of 0.05 after controlling the false discovery rate (Benjamini and Hochberg, 1995; Wilks, 2016); the two-tailed p values are generated by Welch's unequal variances t-test, using annual mean data from each simulation year as the input; the approximate p value threshold, p_{FDR}, which takes the false discovery rate into account, is written underneath each map. The analysis period is 30 years.

Total organic carbon aerosol column burden ($Burden_{OC}$)
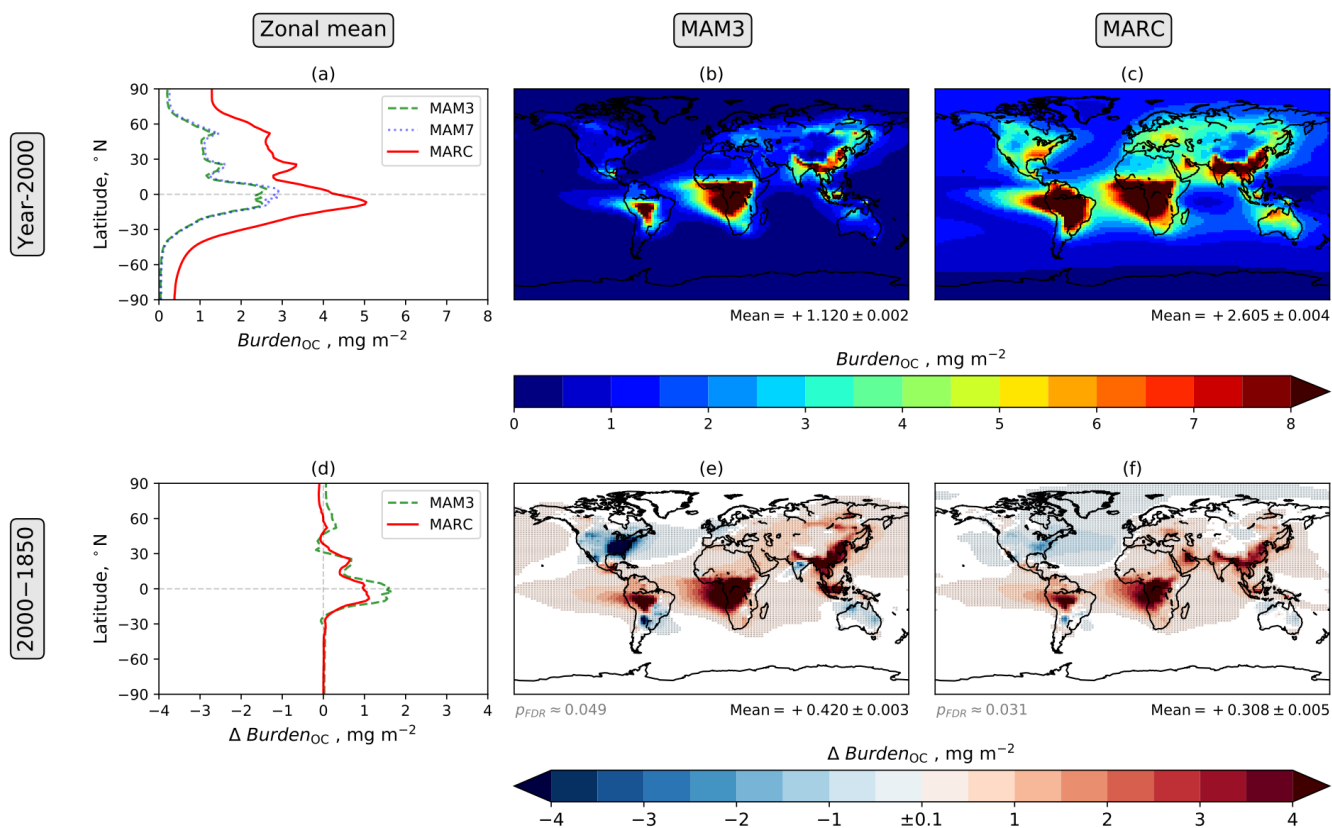
Figure 2: **Annual mean total organic carbon aerosol burden ($Burden_{OC}$). MARC does not directly diagnose total organic carbon aerosol burden, so we have used the mass-mixing ratios diagnosed by MARC in order to calculate the total organic carbon aerosol burden – the errors associated with this post-processing step are estimated to be less than 1% for all grid-boxes, and the errors are far smaller when global mean averaging is applied. The figure components are explained in the Fig. 1 caption.**

Figure 3: Annual mean total black carbon aerosol burden ($Burden_{BC}$). MARC does not directly diagnose total black carbon aerosol burden, so we have used the mass-mixing ratios diagnosed by MARC in order to calculate the total black carbon aerosol burden. The figure components are explained in the Fig. 1 caption.

5

Atmospheric
Chemistry
and Physics
Discussions

Total sea salt aerosol column burden ($Burden_{salt}$)
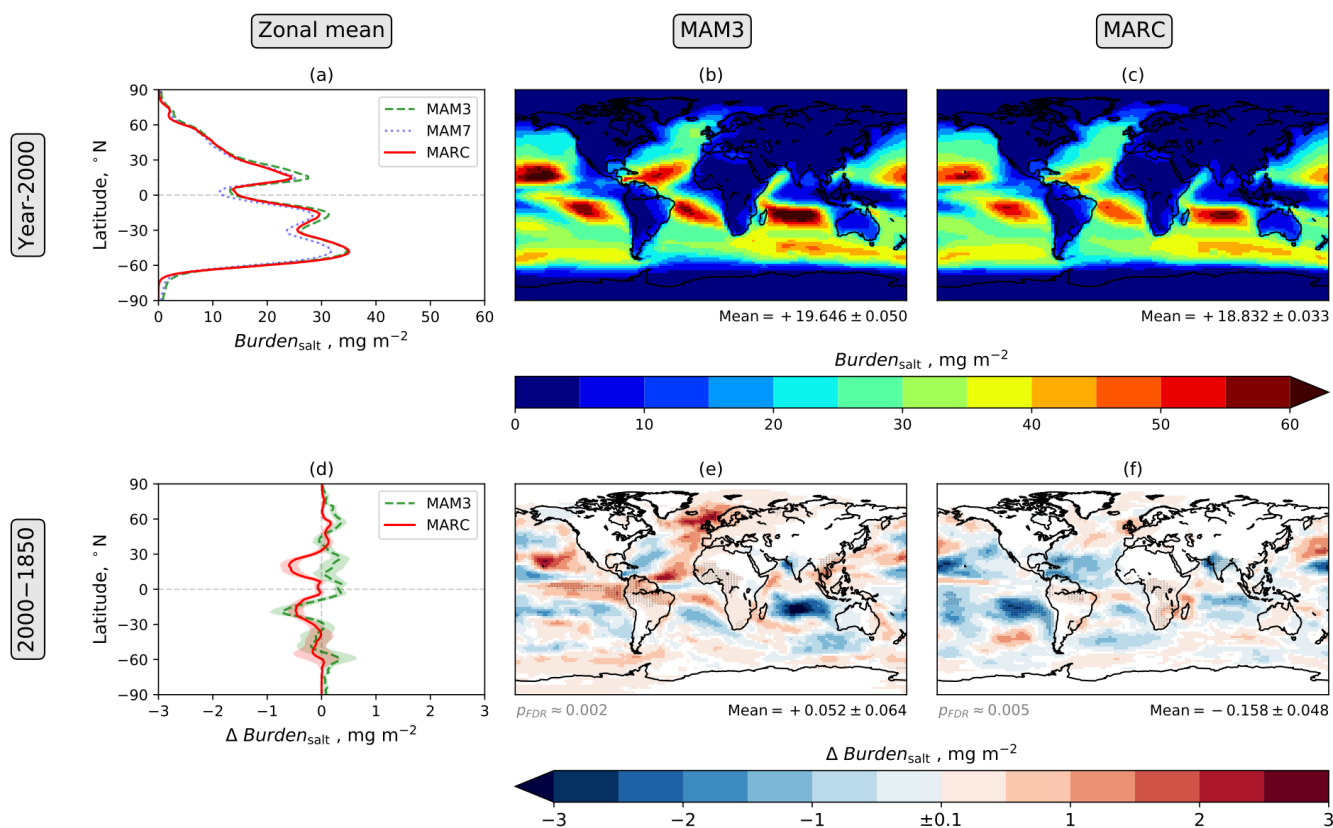
Figure 4: Annual mean total sea salt aerosol burden ($Burden_{salt}$). MARC does not directly diagnose sea salt aerosol burden, so we have used the mass-mixing ratios diagnosed by MARC in order to calculate the total sea salt aerosol burden. The figure components are explained in the Fig. 1 caption.

5
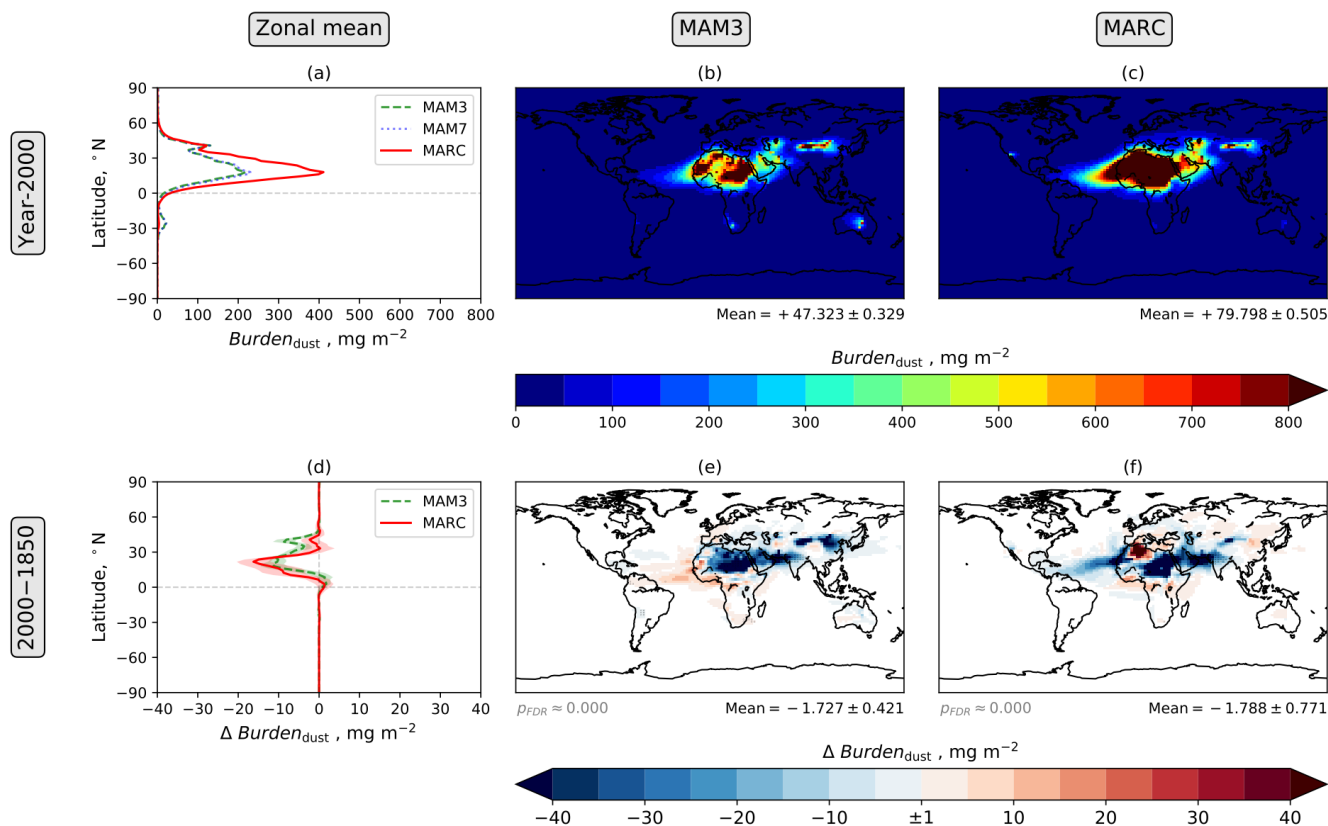
Figure 5: Annual mean dust aerosol burden ($Burden_{dust}$). MARC does not directly diagnose dust aerosol burden, so we have used the mass-mixing ratios diagnosed by MARC in order to calculate the total dust aerosol burden. The figure components are explained in the Fig. 1 caption.

5
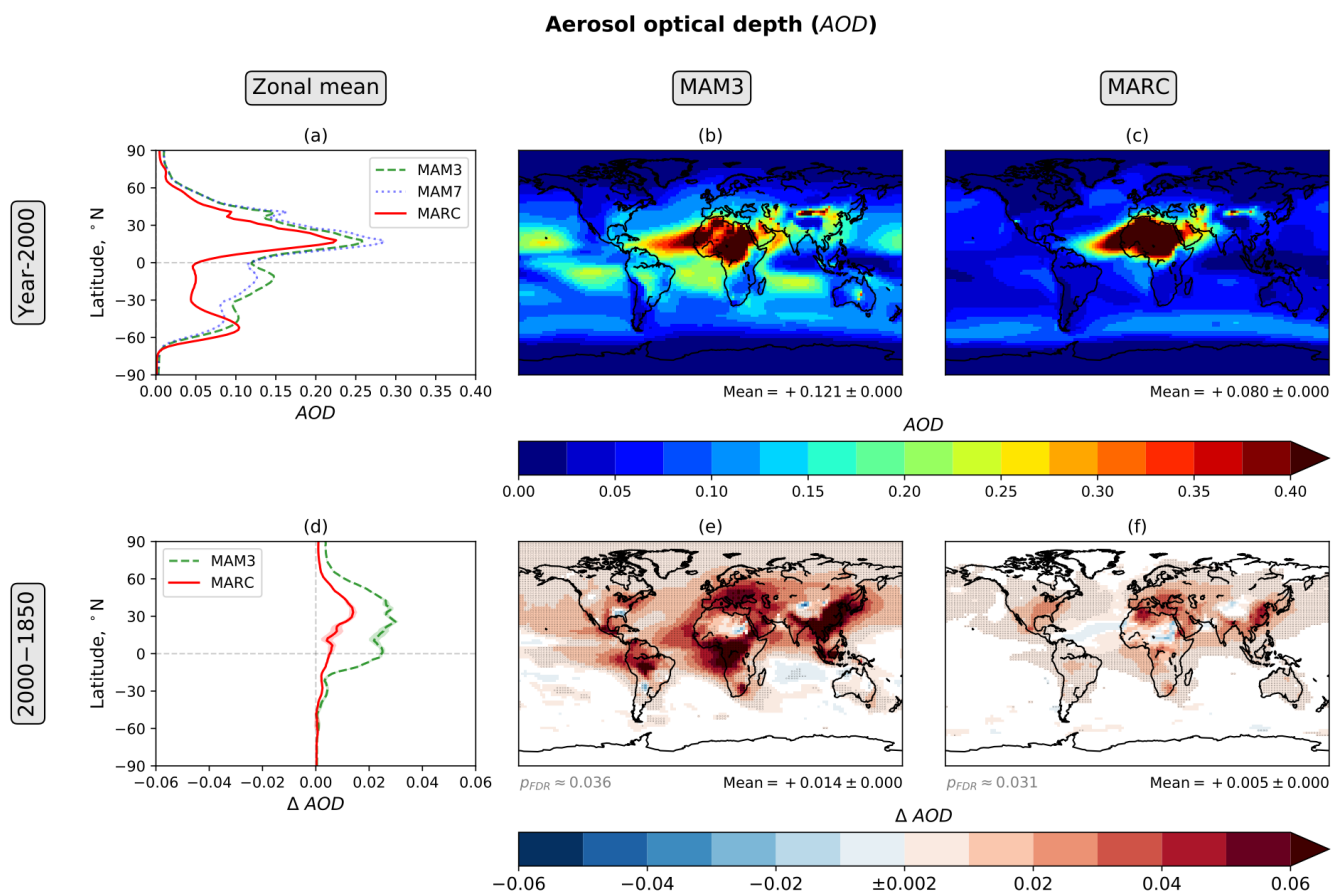
Figure 6: Annual mean aerosol optical depth (*AOD*). The figure components are explained in the Fig. 1 caption.
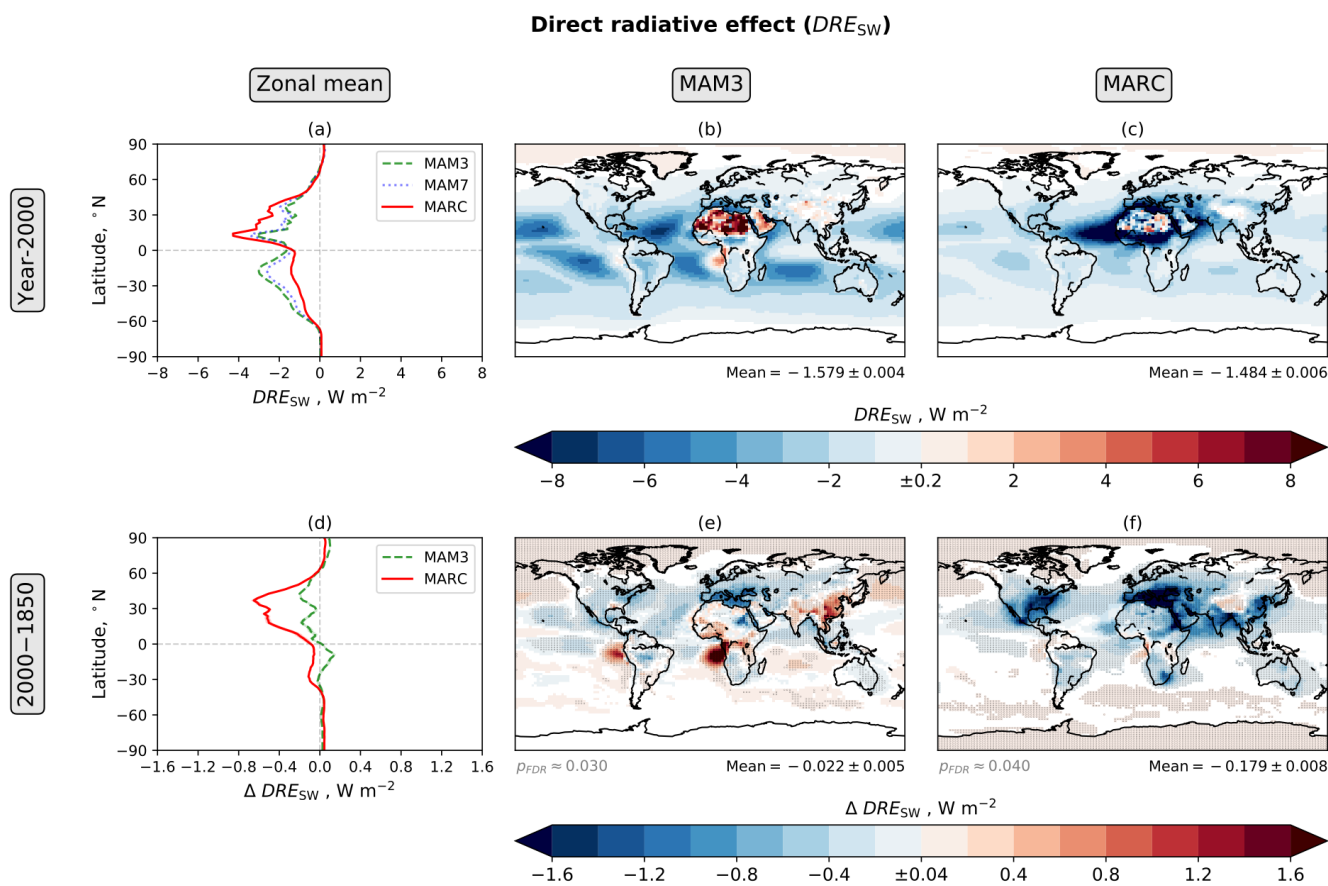
Figure 7: Annual mean direct radiative effect (DRE_{SW}; Eq. (3)). The figure components are explained in the Fig. 1 caption. For all four maps, white indicates differences with a magnitude less than the threshold value in the centre of the corresponding colour bar.

5
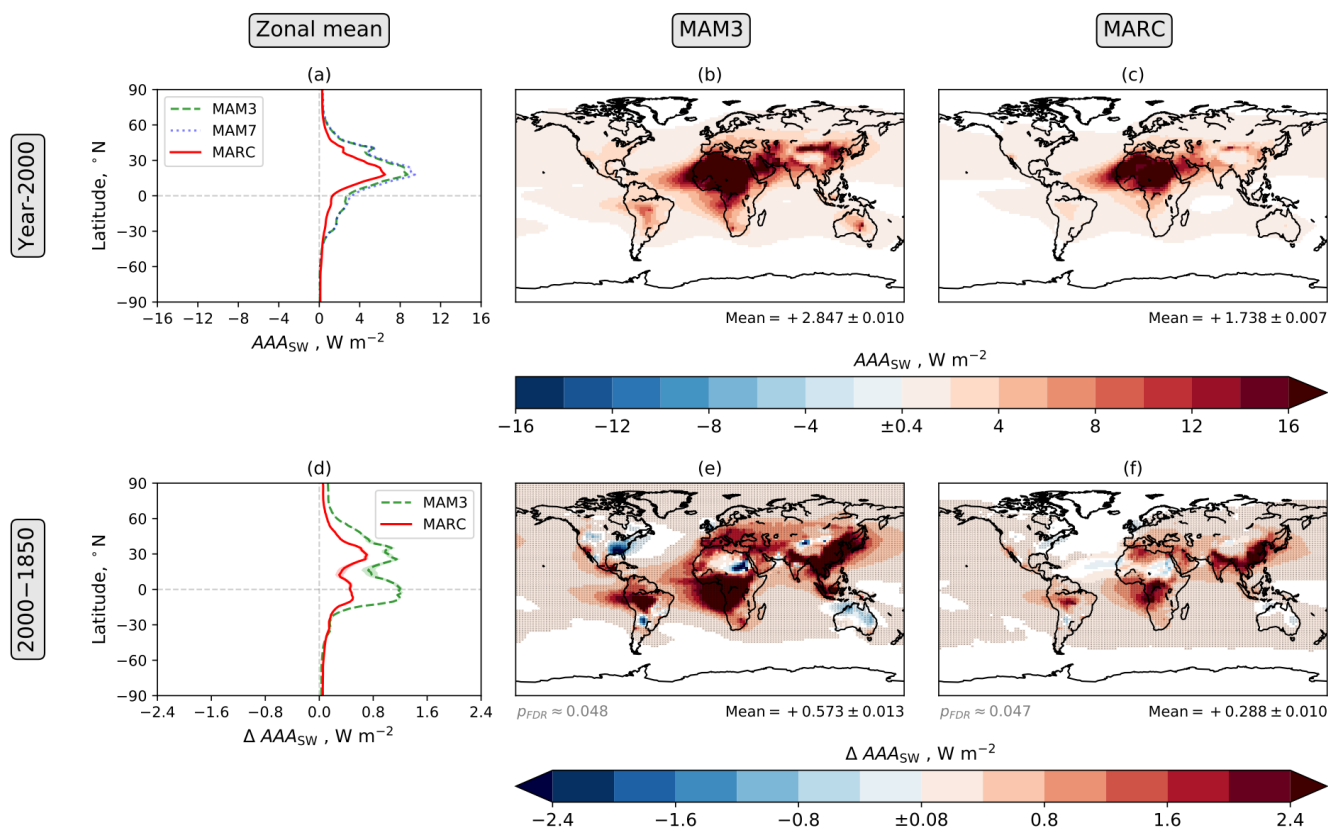
Figure 8: Annual mean absorption by aerosols in the atmosphere (AAA_{SW}; Eq. (8)). The figure components are explained in the Fig. 1 caption. For all four maps, white indicates differences with a magnitude less than the threshold value in the centre of the corresponding colour bar.

5

Cloud condensation nuclei concentration at 0.1% supersaturation (CCN_{conc}) in model level 24 (~860hPa)
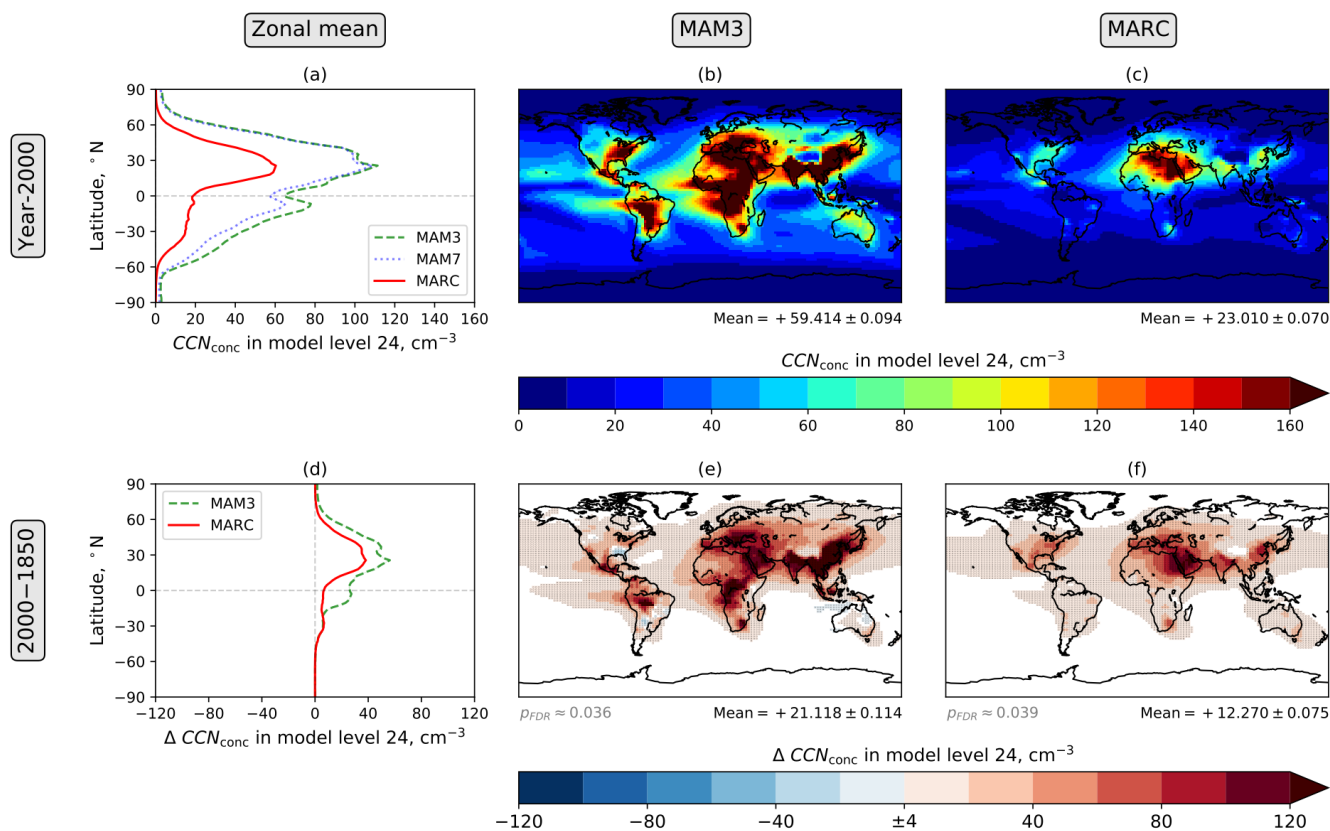
Figure 9: Annual mean cloud condensation nuclei concentration at 0.1% supersaturation (CCN_{conc}) in model level 24 (in the lower troposphere). The figure components are explained in the Fig. 1 caption. Corresponding results, showing CCN_{conc} near the surface and in the mid-troposphere (model level 19), are shown in Figs. S1 and S2 of the Supplement.

5
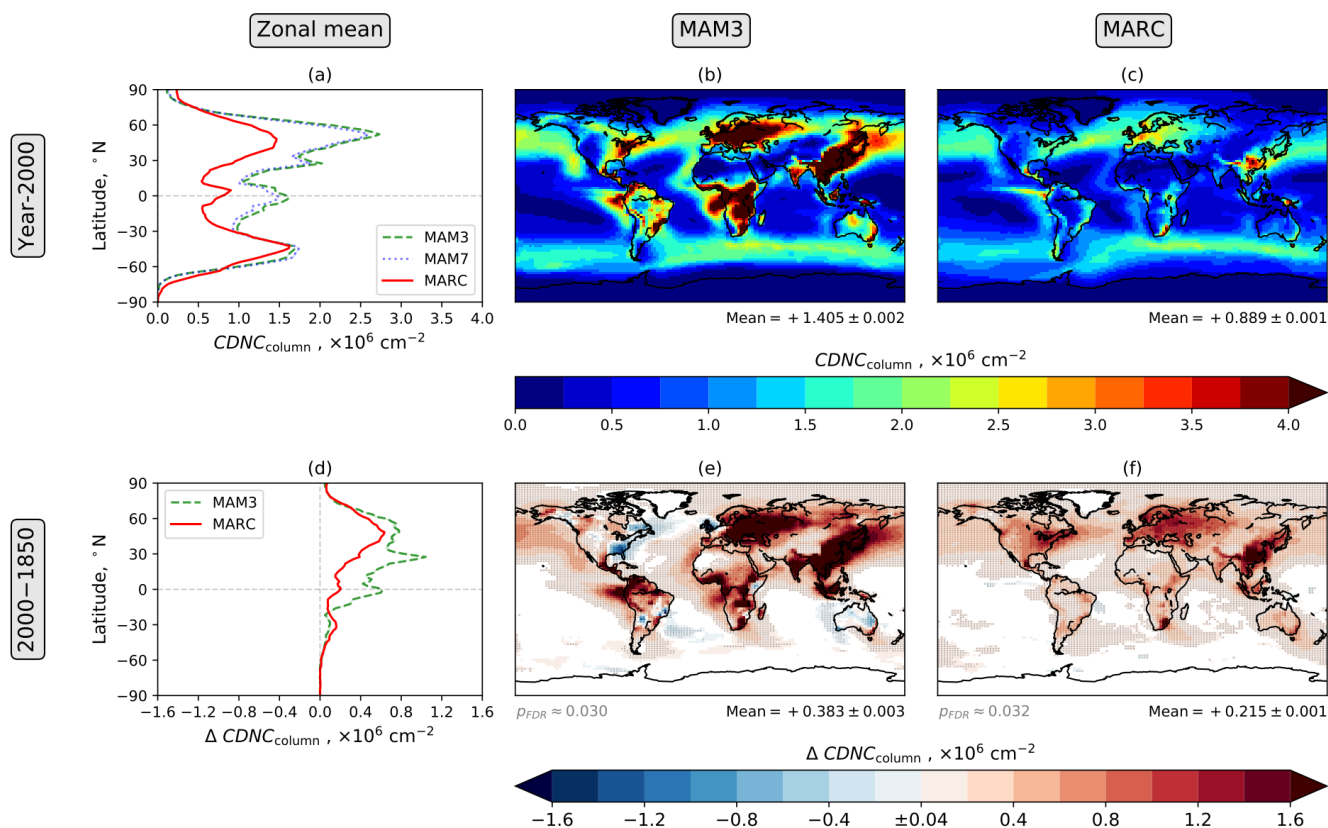
Figure 10: Annual mean column-integrated cloud droplet number concentration ($CDNC_{\text{column}}$). **The figure components are explained in the Fig. 1 caption.**
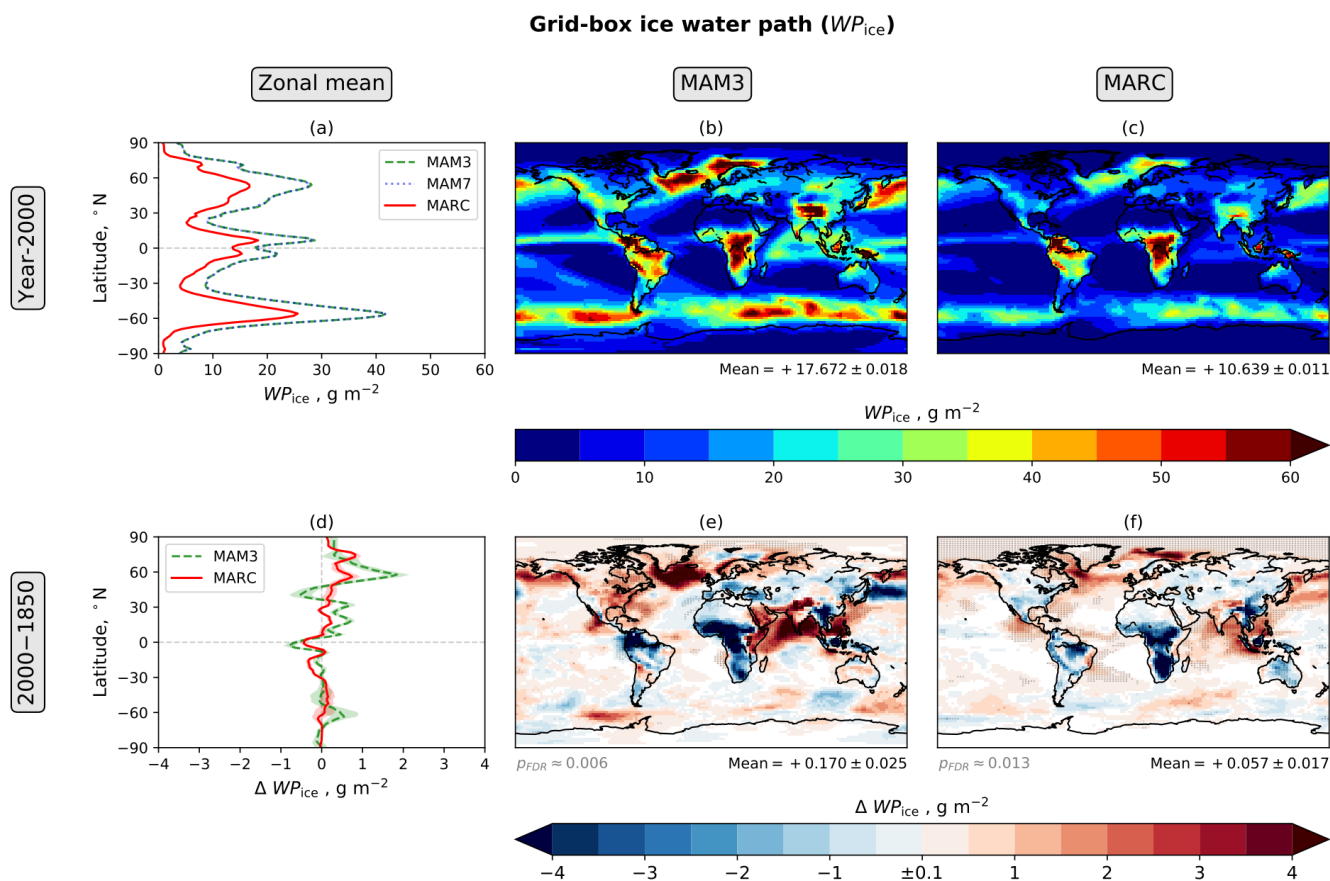
Grid-box liquid water path (WP_{liquid})
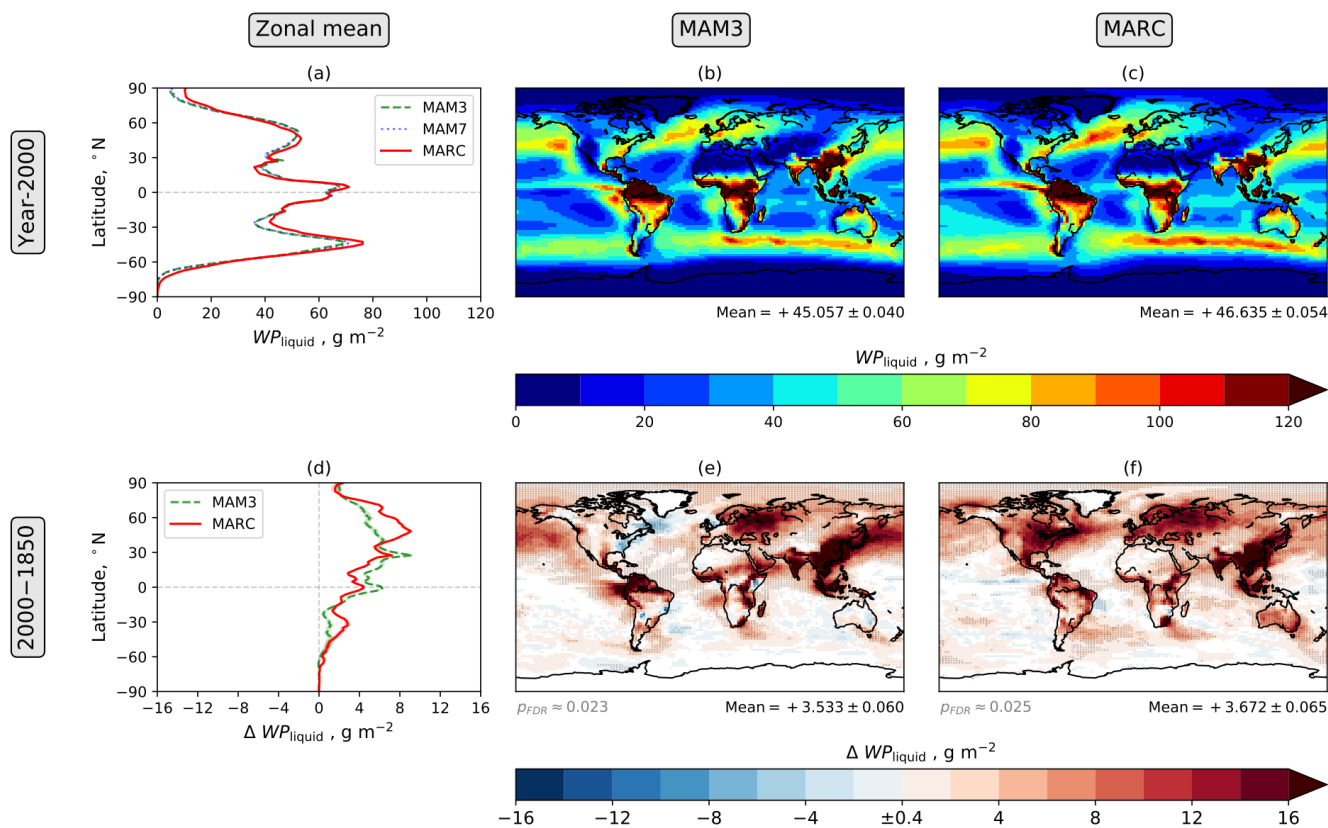
Figure 11: **Annual mean grid-box cloud liquid water path (WP_{liquid}). The figure components are explained in the Fig. 1 caption.**

Grid-box ice water path (WP_{ice})

Figure 12: Annual mean grid-box cloud ice water path (WP_{ice}). The figure components are explained in the Fig. 1 caption.
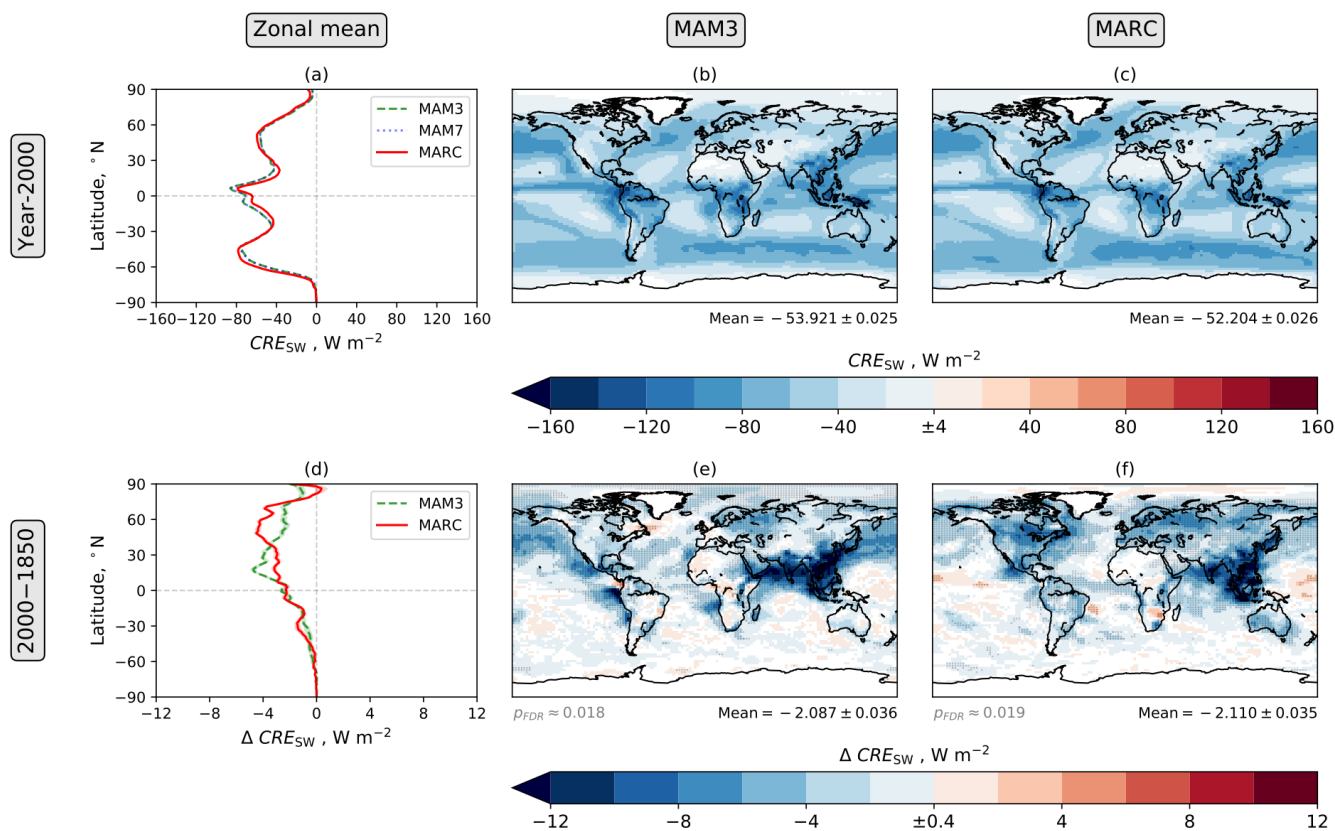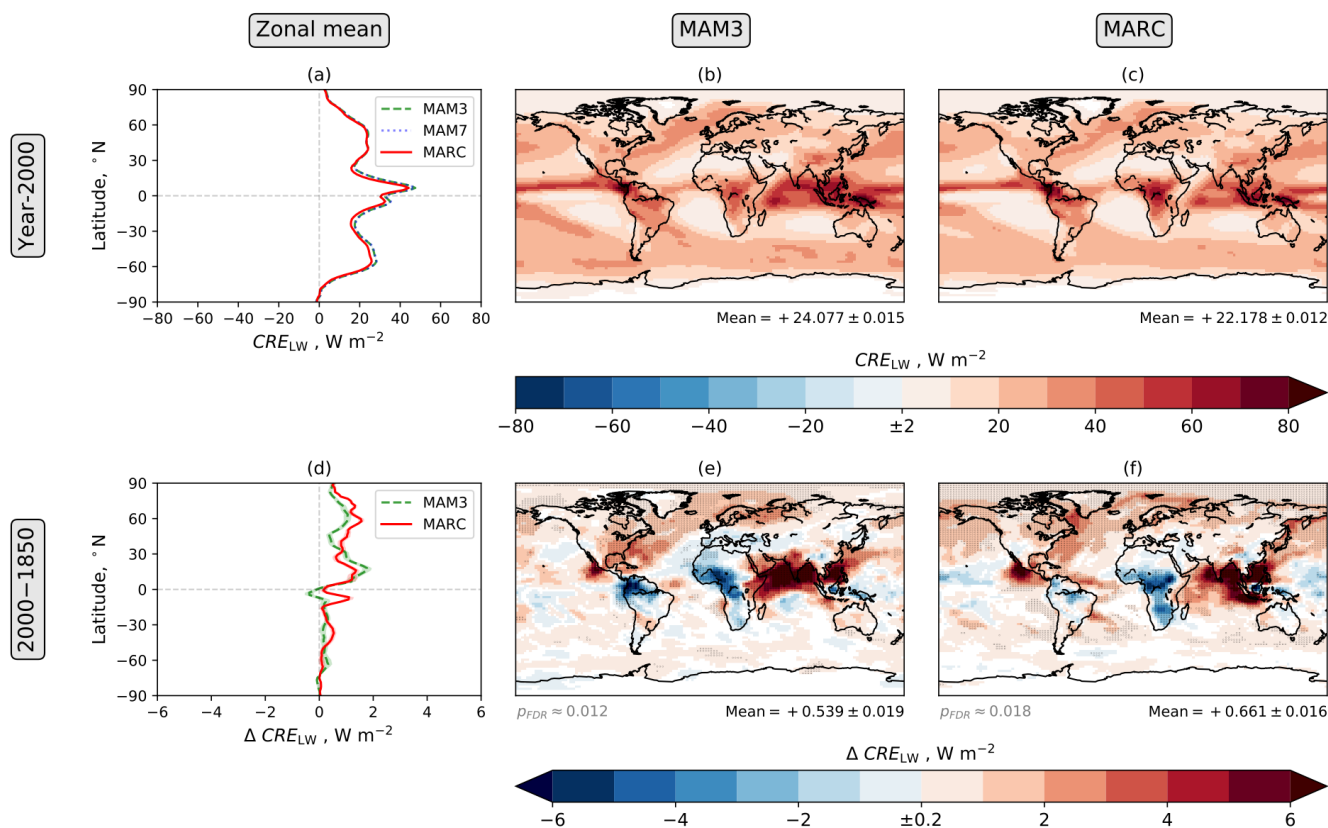
Figure 13: **Annual mean clean-sky shortwave cloud radiative effect (CRE_{SW}; Eq. (4)). The figure components are explained in the Fig. 1 caption. For all four maps, white indicates differences with a magnitude less than the threshold value in the centre of the corresponding colour bar.**

5

Atmospheric
Chemistry
and Physics
Discussions

Longwave cloud radiative effect (CRE_{LW})

Figure 14: Annual mean longwave cloud radiative effect (CRE_{LW}; Eq. (6)). The figure components are explained in the Fig. 1 caption. For all four maps, white indicates differences with a magnitude less than the threshold value in the centre of the corresponding colour bar.

5

Δ surface albedo radiative effect (ΔSRE$_{SW}$)
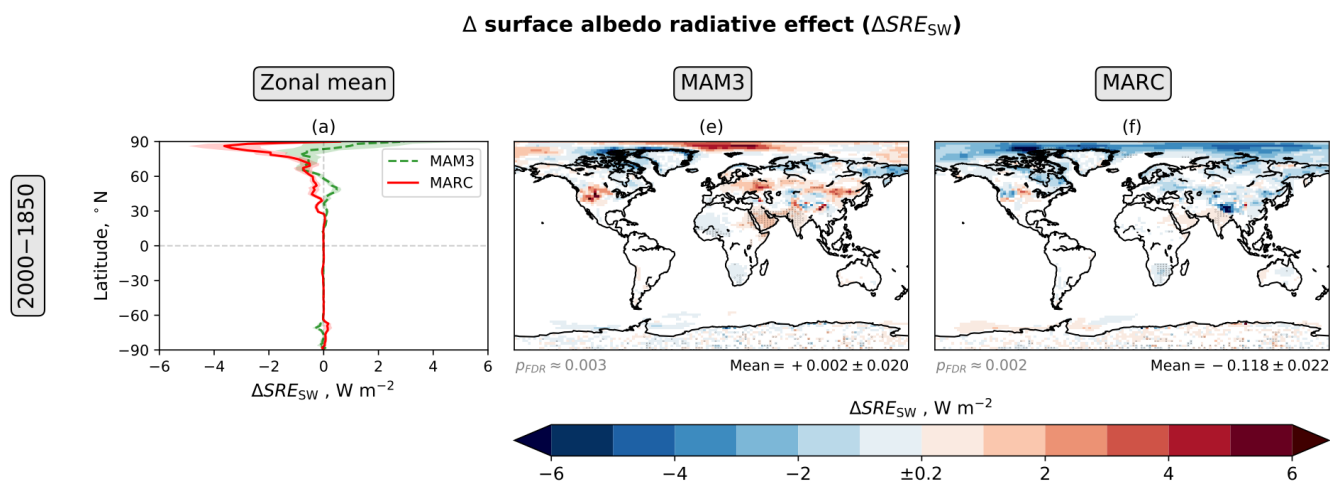
Figure 15: Annual mean 2000-1850 surface albedo radiative effect (ΔSRE_{SW}; Eq. (5)). The figure components are explained in the Fig. 1 caption.

5

Net effective radiative forcing (ERF$_{SW+LW}$)
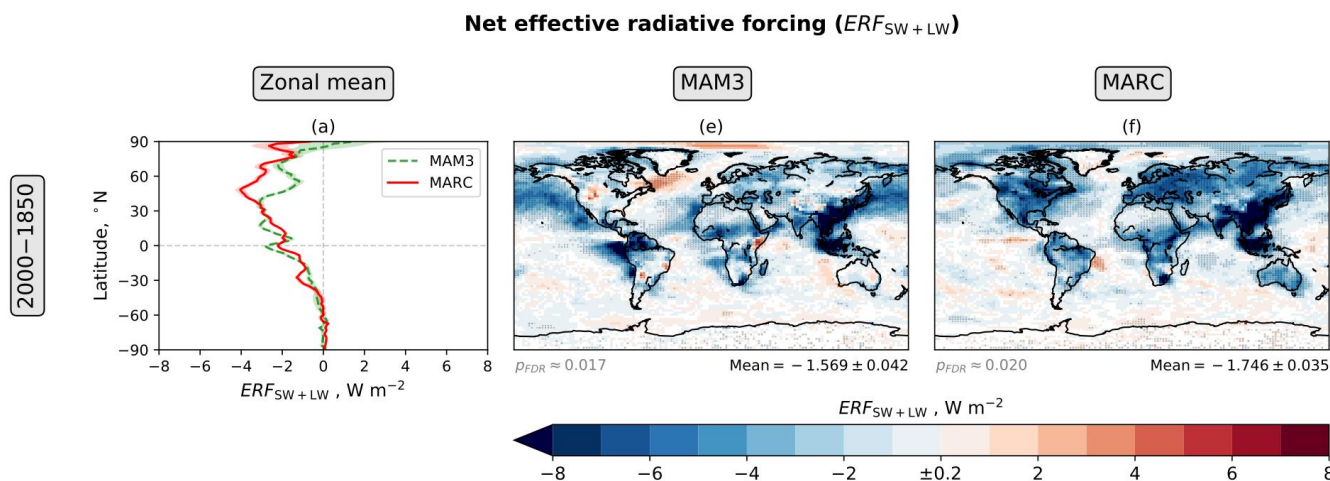
Figure 16: Annual mean 2000-1850 net effective radiative forcing (ERF_{SW+LW}; Eq. (7)). The figure components are explained in the Fig. 1 caption. When comparing the relative contributions of the different radiative effect components to ERF_{SW+LW}, note that
10 different colour bars are used in Figs. 7, 13, 14, 15, and 16.